PHASE BEHAVIOR OF DIPOLAR FLUIDS AND ION–DIPOLE MIXTURES, AND SURFACE DIFFUSION OF ADSORBED POLYMERS

BY

WON KI ROH

DISSERTATION

Submitted in partial fulfillment of the requirements
for the degree of Doctor of Philosophy in Materials Science and Engineering
in the Graduate College of the
University of Illinois at Urbana-Champaign, 2010

Urbana, Illinois

Doctoral Committee:

Associate Professor Erik Luijten, Chair
Professor Kenneth S. Schweizer
Professor Gerard C. L. Wong
Professor Kyekyoon Kim

ABSTRACT

Dipole moments are ubiquitous in nature. Studying dipole moments is the first step toward understanding phase behavior of various colloids with strong dipole moments. Since the Dipolar Hard Sphere fluid (DHS) is the simplest model described by dipolar interactions, studying this model is fundamentally important for understanding the structures and thermodynamics of polar fluids. A variety of unsolved scientific questions arises when the dimensionality of this model is changed and when other species are introduced in this model. Finally, the last part of this dissertation discusses the diffusion behavior of adsorbed polymers over the full concentration range.

In Chapter 2, I study the phase behavior of dipolar fluids by means of Monte Carlo simulations. My goal in this chapter is to examine the possibility of phase separation in a dipolar fluid system and to use quantitative structural information to shed light on this controversy. How dimensionality affects the phase behavior of dipolar fluids is also an interesting question. Thus, in Chapter 3, I examine the possibility of phase separation in quasi-2-dimensional dipolar fluids. In Chapter 4, I proceed to binary systems. Since I have excluded the possibility of phase separation in the DHS system and it is well known that the RPM system exhibits phase separation, these results naturally lead to the question whether phase separation takes place in mixtures that contain ions as well as dipolar particles. I map out the phase diagrams by varying the strength ratio of the dipolar to the ionic interaction and I also locate the critical points.

In Chapter 5, I turn to a rather different research topic, namely the dynamics of adsorbed polymers. I employ molecular dynamics to investigate the relation between surface diffusion and conformation of adsorbed polymers over the full coverage range.

To my family

ACKNOWLEDGMENTS

Completing this dissertation would not have been possible without the help and support of many people. I thank my advisor Erik Luijten for his guidance and critical eye. I also thank the members of my committee, Kenneth Schweizer, Gerard Wong, and Kyekyoon Kim for their advice. Thanks to my group members—especially, Kipton Barros—for many discussions, and Korean friends for making my time in Urbana–Champaign a memorable experience. Finally, many thanks to my family for their love and unconditional support. Especially, thanks to my wife Eunju Jeong who always encourages and comforts me whenever I am in trouble. I also thank my son Hyunseok who gives me a bright smile and a warm hug every morning.

TABLE OF CONTENTS

Chapter 1 Introduction 1
1.1 References 3

Chapter 2 Dipolar Hard-Sphere Fluid 7
2.1 Simulation methodology 7
2.2 Density distribution 11
2.3 Specific heat 13
2.4 Compressibility 16
2.5 Structure 17
2.6 Summary and conclusions 21
2.7 References 22

Chapter 3 Quasi-2-Dimensional Dipolar Hard-Sphere Fluid 26
3.1 Simulation methodology 26
3.2 Thermodynamic properties 27
3.3 Summary and conclusions 32
3.4 References 33

Chapter 4 Ion–Dipole Mixtures 35
4.1 Simulation methodology 35
4.2 Demixing with zero or weak dipole moment 37
4.3 Ionic phase separation with intermediate dipole moment 39
4.4 Phase separation with strong dipole moment 43
4.5 Structure 46
4.6 Summary and conclusions 47
4.7 References 48

Chapter 5 Diffusion of Adsorbed Polymers 51
5.1 Simulation methodology 52
5.2 Diffusion coefficient 56
5.3 Summary and conclusions 59
5.4 References 60

Author's biography 63

CHAPTER 1

INTRODUCTION

Dipole moments are ubiquitous in nature. Studying dipole moments is the first step toward understanding phase behavior of various colloids with strong dipole moments [1–4]. Since the Dipolar Hard Sphere fluid (DHS) is the simplest model described by dipolar interactions, studying this model is fundamentally important for understanding the structures and thermodynamics of polar fluids. A variety of unsolved scientific questions arises when the dimensionality of this model is changed and when other species are introduced in this model. In this dissertation I present the results of simulation research on the phase behavior of the DHS in three-dimensional (3D) and two-dimensional (2D) space, and on mixtures that contain ions as well as dipoles. Furthermore, the last part of this dissertation discusses the diffusion behavior of adsorbed polymers over the full concentration range, from the dilute to the concentrated regime.

This thesis is organized as follows: In Chapter 2, I study the phase behavior of dipolar fluids by means of Monte Carlo simulations. It is well established that simple fluids can exhibit a liquid–vapor phase transition due to short-range van der Waals attractions [5]. Coulombic interactions can also induce phase separation in ionic solutions [6, 7]. By contrast, the occurrence of liquid–vapor phase separation driven by anisotropic dipolar interactions is still a matter of debate. Although de Gennes and Pincus suggested the possibility of such a phase transition in dipolar fluids [8], evidence for a liquid–vapor phase transition in this system has been hardly found in various simulation studies [9–14]. Interestingly, however, Camp *et al.* found evidence from grand-canonical Monte Carlo simulations that the dipolar fluid may have a liquid–vapor phase transition [14]. In the same paper, their results were confirmed by independent NPT and NVT simulations. My goal in this chapter is to examine the possibility of phase separation in a dipolar fluid system and to use quantitative structural information to shed light on this controversy.

In Chapter 3, I examine the possibility of phase separation in quasi-2D dipolar fluids. In quasi-

2D systems the centers of the dipolar spheres are confined to a plane; however, the dipole moments can rotate in full 3D space. Studying this system can be a potential starting point to understand the appearance of unexpected stripe patterns of dipolar nanorods in a plane [3]. Furthermore, the fact that Coulombic interactions in different dimensions can induce different types of phase separation [6, 7, 15–20] introduces an interesting question regarding how dimensionality affects the phase behavior of dipolar fluids. The simulation results of the previous chapter for the 3D DHS system exclude the possibility of liquid–vapor phase separation for a large region of the temperature–density plane, whereas theory has predicted that 2D dipolar disks undergo phase separation [21]. In the quasi-2D DHS model [22, 23], the occurrence of phase separation is still an open question, and I want to contribute to this problem.

In Chapter 4, I proceed to binary systems. Since I have excluded the possibility of phase separation in the DHS system and it is well known that the RPM system exhibits phase separation, these results naturally lead to the question whether phase separation takes place in mixtures that contain ions as well as dipolar particles. According to the Gibbs phase rule, adding one more component gives one additional degree of freedom and leads to a more complex phase diagram [24–28]. It is also known [25–27] that the van der Waals (vdW) equation of state exhibits six principal classes of phase diagram when the parameters of the vdW model are varied, and most of these predicted phase diagrams have been discovered experimentally. However, phase behavior of ion–dipole binary systems is not fully understood yet. Therefore, I hope to improve our understanding of the phase diagrams of ion–dipole mixtures and the influence of physical parameters (ion charge and dipole moment) on the topologies of these phase diagrams. Because of the complexity of multicomponent systems, mapping out the entire phase diagram for these mixtures would take a prohibitive amount of simulation time. Instead, I have opted to focus on the most interesting temperature for this mixture. Then, I map out the phase diagrams by varying the strength ratio of the dipolar to the ionic interaction and I also locate the critical points.

In Chapter 5, I turn to a rather different research topic, namely the dynamics of adsorbed polymers. Studying the behavior of polymers near surfaces is important because it is applicable to surface coating, adhesives and tribology, and because it helps to understand a basic property of polymers [29–32]. Recently, intensive efforts have been made to understand surface diffusion properties of polymers, both by experiments [33–38] and by simulations [39–45]. Even though the effect

of the presence of multiple chains on the polymer dynamics near a surface is a fundamentally important question, existing simulation studies only focus on single-polymer behavior in the dilute regime. In 2004, Zhao and Granick investigated polymer lateral diffusion as a function of surface coverage [46]. Their results showed that the lateral diffusion coefficient increases with increasing surface coverage until monolayer coverage is reached, followed by an abrupt decrease in the diffusion rate. This anomalous behavior is possibly related to conformational changes, but this cannot be confirmed in the experimental setup. In this chapter, I employ molecular dynamics to investigate the relation between surface diffusion and conformation of adsorbed polymers over the full coverage range.

1.1 References

[1] M. Klokkenburg, C. Vonk, E. M. Claesson, J. D. Meeldijk, B. H. Erné and A. P. Philipse, "Direct imaging of zero-field dipolar structures in colloidal dispersions of synthetic magnetite," J. Am. Chem. Soc. **126**, 16706–16707 (2004).

[2] M. Klokkenburg, C. Vonk, E. M. Claesson, J. D. Meeldijk, B. H. Erné and A. P. Philipse, "Quantitative real-space analysis of self-assembled structures of magnetic dipolar colloids," Phys. Rev. Lett. **96**, 037203 (2006).

[3] A. Ghezelbash, B. Koo and B. A. Korgel, "Self-assembled stripe patterns of CdS nanorods," Nano Letters **6**, 1832–1836 (2006).

[4] S. Gupta, Q. Zhang, T. Emrick and T. P. Russell, ""Self-corralling" nanorods under an applied electric field," Nano Letters **6**, 2066–2069 (2006).

[5] J. J. Nicolas, K. E. Gubbins, W. B. Streett and D. J. Tildesley, "Equation of state for the Lennard-Jones fluid," Mol. Phys. **37**, 1429–1454 (1979).

[6] G. Orkoulas and A. Z. Panagiotopoulos, "Free energy and phase equilibria for the restricted primitive model of ionic fluids from Monte Carlo simulations," J. Chem. Phys. **101**, 1452–1459 (1994).

[7] E. Luijten, M. E. Fisher and A. Z. Panagiotopoulos, "Universality class of criticality in the restricted primitive model electrolyte," Phys. Rev. Lett. **88**, 185701 (2002).

[8] P. G. de Gennes and P. A. Pincus, "Pair correlations in a ferromagnetic colloid," Phys. Kondens. Mater. **11**, 189–198 (1970).

[9] J.-M. Caillol, "Search of the gas–liquid transition of dipolar hard spheres," J. Chem. Phys. **98**, 9835–9849 (1993).

[10] J. J. Weis and D. Levesque, "Chain formation in low density dipolar hard spheres: A Monte Carlo study," Phys. Rev. Lett. **71**, 2729–2732 (1993).

[11] M. E. van Leeuwen and B. Smit, "What makes a polar liquid a liquid?," Phys. Rev. Lett. **71**, 3991–3994 (1993).

[12] S. C. McGrother and G. Jackson, "Island of vapor-liquid coexistence in dipolar hard-core systems," Phys. Rev. Lett. **76**, 4183–4186 (1996).

[13] J. C. Shelley, G. N. Patey, D. Levesque and J. J. Weis, "Liquid-vapor coexistence in fluids of dipolar hard dumbbells and spherocylinders," Phys. Rev. E **59**, 3065–3070 (1999).

[14] P. J. Camp, J. C. Shelley and G. N. Patey, "Isotropic fluid phases of dipolar hard spheres," Phys. Rev. Lett. **84**, 115–118 (2000).

[15] E. Luijten, M. E. Fisher and A. Z. Panagiotopoulos, "The heat capacity of the restricted primitive model electrolyte," J. Chem. Phys. **114**, 5468–5471 (2001).

[16] J. J. Weis, D. Levesque and J. M. Caillol, "Restricted primitive model of an ionic solution confined to a plane," J. Chem. Phys. **109**, 7486–7496 (1998).

[17] G. Orkoulas and A. Z. Panagiotopoulos, "Phase diagram of the two-dimensional Coulomb gas: A thermodynamic scaling Monte Carlo study," J. Chem. Phys. **104**, 7205–7209 (1996).

[18] J. Lidmar and M. Wallin, "Monte Carlo simulation of a two-dimensional continuum Coulomb gas," Phys. Rev. B **55**, 522–530 (1997).

[19] E. Lomba, J. J. Weis and F. Lado, "Structure and thermodynamics of a two-dimensional Coulomb fluid in the strong association regime," J. Chem. Phys. **127**, 074501 (2007).

[20] A. R. Mehrabi and M. Sahimi, "Cluster conformations and multipole distributions in ionic fluids. I. Two-dimensional systems of mobile ions," J. Chem. Phys. **128**, 234503 (2008).

[21] G. P. Morris and J. W. Perram, "The dielectric constant of dipolar discs," Physica **129A**, 395–407 (1985).

[22] J. M. Tavares, J. J. Weis and M. M. Telo da Gama, "Quasi-two-dimensional dipolar fluid at low densities: Monte Carlo simulations and theory," Phys. Rev. E **65**, 061201 (2002).

[23] J. M. Tavares, J. J. Weis and M. M. Telo da Gama, "Phase transition in two-dimensional dipolar fluids at low densities," Phys. Rev. E **73**, 041507 (2006).

[24] J. J. van Laar, "On the different forms and transformations of the boundary-curves in the case of partial miscibility of two liquids," Proc. Kon. Akad. **7**, 636–645 (1905).

[25] R. L. Scott and P. H. Van Konynenburg, "Van der Waals and related models for Hydrocarbon mixtures," Discuss. Faraday Soc. **49**, 87–97 (1970).

[26] P. H. Van Konynenburg and R. L. Scott, "Critical lines and phase equilibria in binary Van der Waals mixtures," Phil. Trans. Roy. Soc. London **298**, 495–540 (1980).

[27] J. S. Rowlinson and F. L. Swinton, *Liquids and liquid mixtures*, 3rd ed. (Butterworths, London, 1982).

[28] R. L. Scott, "Models for phase equilibria in fluid mixtures," Acc. Chem. Res. **20**, 97–107 (1987).

[29] R. P. Wool, *Polymer Interfaces: Structure and Strength* (Hanser Gardner Publications, Cincinnati, 1994).

[30] Z. W. Wicks, F. N. Jones and S. P. Pappas, *Organic Coatings: Science and Technology* (A Wiley-Interscience, New York, 1999).

[31] G. J. Fleer, M. A. Cohen Stuart, J. M. H. M. Scheutjens, T. Cosgrove and B. Vincent, *Polymers at interfaces* (Chapman & Hall, London, 1993).

[32] R. A. L. Jones and R. W. Richards, *Polymers at surfaces and interfaces* (Cambridge University Press, Cambridge, 1999).

[33] B. Maier and J. O. Rädler, "Conformation and self-diffusion of single DNA molecules confined to two dimensions," Phys. Rev. Lett. **82**, 1911–1914 (1999).

[34] B. Maier and J. O. Rädler, "DNA on fluid membranes: A model polymer in two dimensions," Macromolecules **33**, 7185–7194 (2000).

[35] S. A. Sukhishvili, Y. Chen, J. D. Müller, E. Gratton, K. S. Schweizer and S. Granick, "Diffusion of a polymer 'pancake'," Nature **406**, 146 (2000).

[36] S. A. Sukhishvili, Y. Chen, J. D. Müller, E. Gratton, K. S. Schweizer and S. Granick, "Surface diffusion of poly(ethylene glycol)," Macromolecules **35**, 1776–1784 (2002).

[37] L. Zhang and S. Granick, "Slaved diffusion in phospholipid bilayers," Proc. Natl. Acad. Sci. U.S.A. **102**, 9118–9121 (2005).

[38] D. Nykypanchuk, H. H. Strey and D. A. Hoagland, "Brownian motion of DNA confined within a two-dimensional array," Science **297**, 987–990 (2002).

[39] A. Milchev and K. Binder, "Static and dynamic properties of adsorbed chains at surfaces: Monte Carlo simulation of a bead-spring model," Macromolecules **29**, 343–354 (1996).

[40] R. Azuma and H. Takayama, "Diffusion of single long polymers in fixed and low density matrix of obstacles confined to two dimensions," J. Chem. Phys. **111**, 8666–8671 (1999).

[41] A. Sikorski, "Dynamics of adsorbed star-branched polymer chains: A computer simulation study," Macromol. Theory Simul. **12**, 325–331 (2003).

[42] T. G. Desai, P. Keblinski, S. K. Kumar and S. Granick, "Molecular-dynamics simulations of the transport properties of a single polymer chain in two dimensions," J. Chem. Phys. **124**, 084904 (2006).

[43] T. G. Desai, P. Keblinski, S. K. Kumar and S. Granick, "Modeling diffusion of adsorbed polymer with explicit solvent," Phys. Rev. Lett. **98**, 218301 (2007).

[44] H.-J. Qian, L.-J. Chen, Z.-Y. Lu and Z.-S. Li, "Surface diffusion dynamics of a single polymer chain in dilute solution," Phys. Rev. Lett. **99**, 068301 (2007).

[45] D. Mukherji, G. Bartels and M. H. Müser, "Scaling laws of single polymer dynamics near attractive surfaces," Phys. Rev. Lett. **100**, 068301 (2008).

[46] J. Zhao and S. Granick, "Polymer lateral diffusion at the solid–liquid interface," J. Am. Chem. Soc. **126**, 6242–6243 (2004).

CHAPTER 2

DIPOLAR HARD-SPHERE FLUID

The occurrence of liquid–vapor phase separation driven by dipolar interactions is still a controversial topic despite extensive theoretical debate [1–9]. Ng *et al.* published the first simulation study of this system and found phase separation [10]. However, their study is not reliable because they used a very small system size and did not use Ewald summation for long-range dipolar interactions. Furthermore, after this study, extensive simulation efforts have failed to find liquid–vapor phase separation in this system [11–15]. Interestingly, however, Camp *et al.* presented evidence from grand-canonical Monte Carlo (GCMC) simulations for fluid–fluid phase transitions at densities of 0.072 ± 0.008, 0.17 ± 0.02, and 0.28 ± 0.04 at $T^* = 0.14$ [16]. The same paper confirms these findings with independent NPT and NVT simulations. Therefore, I seek to resolve this controversy. To accomplish this goal I implement a biased Monte Carlo (MC) method which samples with high efficiency. Besides, I take advantage of greatly increased computing power compared to what was available several years ago. In this Chapter, I search for evidence of phase separation in dipolar fluids and investigate the structural properties of this system.

2.1 Simulation methodology

The dipolar hard-sphere (DHS) model represents dipolar particles as hard spheres of diameter σ with an embedded central point dipole that can freely rotate in 3D space. The pair potential in the DHS system is expressed by

$$U_{ij} = U_{\mathrm{HS}}(r_{ij}) - \frac{p^2}{4\pi\varepsilon_0\varepsilon r_{ij}^3}[3(\hat{\boldsymbol{p}}_i \cdot \hat{\boldsymbol{r}}_{ij})(\hat{\boldsymbol{p}}_j \cdot \hat{\boldsymbol{r}}_{ij}) - (\hat{\boldsymbol{p}}_i \cdot \hat{\boldsymbol{p}}_j)]\,, \tag{2.1}$$

where $U_{\mathrm{HS}}(r_{ij})$ is the hard-sphere interaction, ε is the dielectric constant of the medium, ε_0 is the dielectric permeability of the vacuum, p is the dipole moment, $\hat{\boldsymbol{p}}_i$ is the unit vector indicating the

dipole orientation of particle i, $\hat{\boldsymbol{r}}_{ij}$ is the unit vector along the interparticle vector $\boldsymbol{r}_{ij}$, and r_{ij} is its magnitude. I use reduced parameters in this study, i.e., I define the reduced density $\rho^* = N\sigma^3/V$, the reduced temperature $T^* = 4\pi\varepsilon_0\varepsilon k_B T\sigma^3/p^2$, the reciprocal temperature $\beta^* = 1/T^*$, the reduced dipole moment $p^* = 1/\sqrt{T^*}$, the reduced chemical potential $\mu^* = \mu T^*/k_B T$, and the reduced system size $L^* = L/\sigma$, where N is the number of dipolar hard spheres in the system, V is the volume of the system, and k_B is Boltzmann's constant. The Ewald summation method is employed for the calculation of long-range dipolar interactions with periodic boundary conditions [17, 18].

To investigate the claim of Camp *et al.* [16], I focus on temperatures in the range $T^* = 0.11$–0.5. I scan the chemical potential at each temperature and find the chemical potentials that produce average number densities in the range of $0.001 \leq \rho^* \leq 0.30$ and simulate longer runs for these chemical potentials to calculate the heat capacity, compressibility and the density distribution of each system. I confirm that the chemical potential in my GCMC code shows good agreement with the calculated chemical potential from the Widom insertion method [18, 19]. I also vary system sizes in the range $L^* = 4$–40 to examine finite-size effects. My simulation is performed using 50% grand-canonical moves and 50% canonical moves, because I find that canonical moves accelerate relaxation of the chain structure. In each MC step, a GCMC move or a canonical move is selected at random. A GCMC move is either an insertion attempt or a deletion attempt, and one canonical move consists of an orientational move of the dipole moment and a translational move with 0.2σ maximum displacement. To examine the efficiency, I determine the required CPU time to obtain one independent sample. My test results show that the combination of half GCMC and half canonical move is 2.2 times more efficient than only GCMC moves at $T^* = 0.20$.

One of the difficulties encountered in simulating the DHS system is the low acceptance rate. Particles have the lowest pair energy ($U = -2\beta^* k_B T$) when they form a head-to-tail conformation. At the critical temperature predicted by Camp *et al.* [16], $T_c^* = 0.15$–0.16, the pair potential is already $-12.5 k_B T$. Therefore, once dipolar hard spheres adopt a chain conformation, it is difficult to insert or delete a particle unless the inserted particle is located near an existing chain or the deleted particle is not part of the chain. To increase the acceptance rate, I use the orientational-bias method, originally developed by Miyatake [20]. In the conventional orientational-bias method, a finite number k of orientations $\{b_1, b_2, \cdots, b_k\}$ for the dipole moment are created instead of one random orientation when a particle insertion is attempted [18]. One of the created orientations is

selected with a probability $P(b_n) = \exp[-\beta U^{\rm or}(b_n)]/\sum_{j=1}^{k}\exp[-\beta U^{\rm or}(b_j)]$, where $U^{\rm or}(b_n)$ is the energy associated with the orientation b_n and $\beta = 1/k_BT$. This probability ensures that a configuration of lower energy is more likely to be selected. However, the drawback of this approach is that additional computing time is required to calculate each of the k different Boltzmann factors. Miyatake suggested an enhancement of this bias method for the Heisenberg spin model [20] and Caillol first used it for the DHS system [11]. Namely, the energy of an inserted dipole in the electric field of all other dipoles in the system can be expressed as the dot product of its dipole moment $\boldsymbol{p}_i$ and the local electric field $\boldsymbol{E}(\boldsymbol{r}_i)$ induced by all other dipoles $\boldsymbol{p}_j$ at position $\boldsymbol{r}_i$,

$$-\boldsymbol{p}_i \cdot \boldsymbol{E}(\boldsymbol{r}_i) = -p\hat{\boldsymbol{p}}_i \cdot \sum_{j=1}^{N}\left[\frac{p}{r_{ij}^3}\{3\hat{\boldsymbol{r}}_{ij}(\hat{\boldsymbol{p}}_j \cdot \hat{\boldsymbol{r}}_{ij}) - \hat{\boldsymbol{p}}_j\}\right]. \tag{2.2}$$

Thus, once $\boldsymbol{E}(\boldsymbol{r}_i)$ is known, the sum of Boltzmann factors can be calculated analytically by integrating over all possible orientations of the dipole,

$$\int_0^{\pi}\exp[\beta\,\boldsymbol{p}_i \cdot \boldsymbol{E}(\boldsymbol{r}_i)]\sin\theta d\theta = \frac{2\sinh[\beta p_i E]}{\beta p_i E}, \tag{2.3}$$

where $p_i = |\boldsymbol{p}_i|$, $E = |\boldsymbol{E}(\boldsymbol{r}_i)|$, and θ denotes the angle between the dipole $\boldsymbol{p}_i$ and the electric field $\boldsymbol{E}(\boldsymbol{r}_i)$. Then, the probability that the dipole is placed under an angle θ with respect to the direction of the electric field follows from

$$P(\theta) = \frac{\exp[\beta p_i E\cos\theta]}{2\sinh[\beta p_i E]/[\beta p_i E]}. \tag{2.4}$$

In the conventional-orientational bias method, increasing the number of created orientations yields a better chance to select a configuration of lower energy. However, more time to generate orientations is needed. In contrast, Eq. 2.4 makes it possible to produce the optimal probability by a single calculation, equivalent to an infinite number of k in the conventional approach. Furthermore, $\cos\theta$ can be chosen according to the above probability from the following equation

$$\cos\theta = \frac{1}{\beta p_i E}\log[2Z\sinh(\beta p_i E) + \exp(-\beta p_i E)], \tag{2.5}$$

where Z is a random number generated uniformly in $0 \le Z \le 1$. Now, energetically favorable con-

figurations are generated frequently; however, the acceptance of this biased generating trial moves should obey detailed balance [18]. Therefore, when imposing detailed balance, an insertion move is selected with a probability

$$P = \min\left[1, \frac{1/2}{P(\theta)} \frac{V}{N+1} \exp(\beta\mu - \beta\Delta U)\right], \tag{2.6}$$

where $P(\theta)$ is the probability to have an angle θ between a dipole moment of an inserted particle i and the electric field and ΔU is the difference in configurational energy ($\Delta U = -\boldsymbol{p}_i \cdot \boldsymbol{E}(\boldsymbol{r}_i)$). The factor $1/2$ indicates the probability of generating a random orientation θ in the ideal gas reservoir representing the inverse probability of grand-canonical move (since $1/\int_0^\pi \sin\theta d\theta = 1/2$). In a similar way, a deletion attempt is accepted with a probability

$$P = \min\left[1, \frac{P(\theta)}{1/2} \frac{N}{V} \exp(-\beta\mu - \beta\Delta U)\right], \tag{2.7}$$

where $P(\theta)$ is the probability to have an angle θ between a dipole moment of a deleted particle i and the electric field and $\Delta U = \boldsymbol{p}_i \cdot \boldsymbol{E}(\boldsymbol{r}_i)$. I also implement the bias method for the canonical ensemble, where the acceptance criterion becomes

$$P = \min\left[1, \frac{P(\theta^{\text{old}})}{P(\theta^{\text{new}})} \exp(-\beta\Delta U)\right], \tag{2.8}$$

where $P(\theta^{\text{new}})$ is the probability of the configuration with an angle θ between a randomly displaced sphere's dipole moment and the electric field and $P(\theta^{\text{old}})$ is the probability of the original configuration. At $T^* = 0.20$, my efficiency test shows that the simulation with the bias method is 3.1 times more efficient than the simulation without biasing.

Typically, 4.0×10^9 MC steps are needed to equilibrate the system at $T^* = 0.14$, $\mu^* = -1.315$ (which corresponds to a density $\rho^* = 0.0555 \pm 0.0004$) and $L^* = 8$, from a random initial configuration. To obtain 5000 independent configurations after equilibration, I simulate 1.0×10^{11} MC steps for the same system. The acceptance rate for the GCMC moves is 0.95% and the acceptance rate for the canonical moves is 15.40% for this system. The total CPU time required to obtain all data at $L^* = 8$, $T^* = 0.14$ is 14800 hours and that at $L^* = 10$, $T^* = 0.14$ is 27900 hours if I use one core of an Intel Xeon EM64T 3.0GHz. In total, I have used $\sim$18 CPU years to perform all

T^*	0.25	0.20	0.18	0.17	0.16
L^*	–	10	12	12	15

Table 2.1: At various temperatures, the largest system size where a density gap still exists is indicated in this table.

simulations for this project.

2.2 Density distribution

I first study the density distribution along isotherms by means of histogram reweighting [21]. If phase separation happens, we expect two distinct peaks in the density distribution if the chemical potential is sufficiently close to its coexistence value. Even though Camp *et al.* [16] found multiple phase transitions at $T^* = 0.14$, my results for $L^* = 8$ [Fig. 2.1(a)] show that the average density increases continuously with increasing chemical potential and that the distribution has a single peak for all simulated chemical potentials. Interestingly, an unexpected gap in the density distribution is observed in the very low-density regime. I find that this gap shows a temperature and system-size dependence. Firstly, the gap becomes shallower with increasing temperature, as seen from Figs. 2.1(a) and (b), which shows the density distribution at$T^* = 0.14$ and $T^* = 0.16$, respectively. I also note that this gap only appears when the average density of the system is low. Secondly, the gap also becomes shallower and eventually even disappears as the system size increases, as verified for $T^* = 0.16$ at $L^* = 10, 12, 15$ (data not shown). Figure 2.1(c) shows the density distributions for $T^* = 0.16$ and $L^* = 20$; it is observed that a gap no longer exists. Table 2.1 shows the largest system size for which a gap exists at various temperatures. When the temperature is higher than $T^* = 0.25$, a gap does not exist even for the smallest simulated system size, $L^* = 4$. For temperatures less than $T^* = 0.16$, system size $L^* = 15$ still shows a gap in the low-density regime.

The location of the sharp peak indicated by the arrows in Fig. 2.1 provides a clue for a possible explanation of this density gap. Namely, the location of the peak equals $\rho^* \approx 1/L^{*2}$. Since my simulations are performed with periodic boundary conditions, the dipolar spheres can align to form an infinite loop parallel to one of the Cartesian axes of the box. The number density at which this chain can form corresponds to the location of the sharp peak. The reason for this behavior

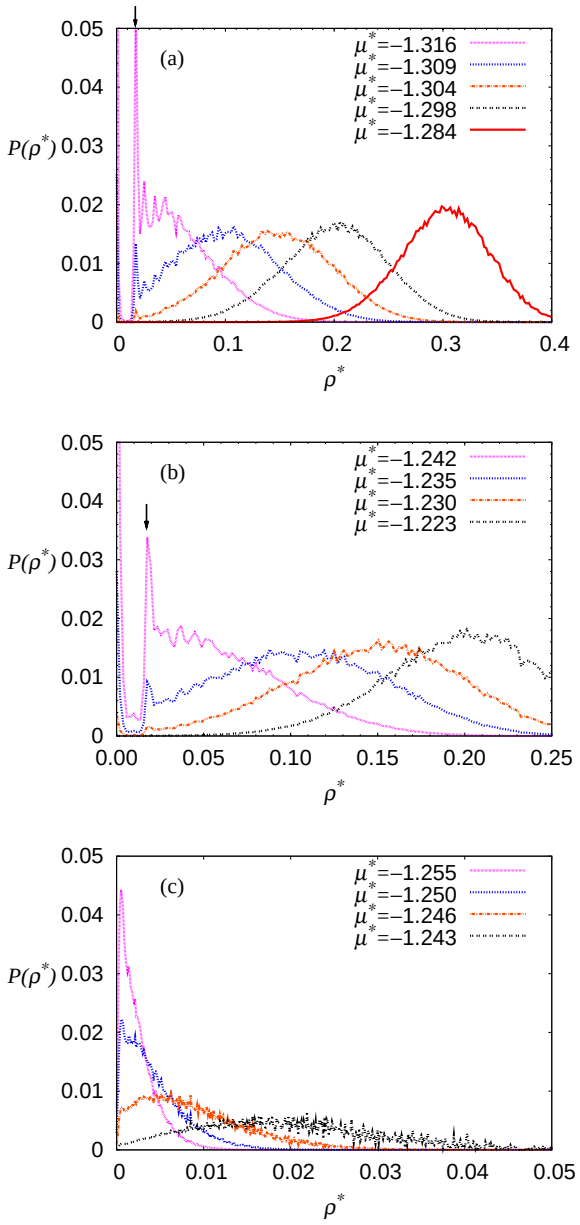

Figure 2.1: The isothermal density distribution of a dipolar hard-sphere fluid at various chemical potentials. The density distribution curves display only one maximum for a fixed chemical potential and shift continuously with changing chemical potential. (a) $T^* = 0.14$ and $L^* = 8$. The density distributions for the chemical potentials $\mu^* = -1.316, -1.309, -1.304, -1.298, -1.284$ correspond to the average densities $\rho^* \approx 0.05, 0.10, 0.15, 0.20, 0.30$, respectively. (b) $T^* = 0.16$ and $L^* = 8$. The density distributions for $\mu^* = -1.242, -1.235, -1.230, -1.223$ represent $\rho^* \approx 0.05, 0.10, 0.15, 0.20$, respectively. (c) $T^* = 0.16$ and $L^* = 20$. The density distributions for $\mu^* = -1.255, -1.250, -1.246, -1.243$ represent $\rho^* \approx 0.002, 0.004, 0.01, 0.02$, respectively.

can be explained as follows. If the simulation box is small, the system can easily lower its energy by forming an infinite loop rather than having a ring or a short chain. For instance, the energy per particle of an infinite loop of 8 particles is $-2.40\beta^* k_B T$, that of a ring of 8 particles is $-2.20\beta^* k_B T$, and that of a finite chain of 4 particles is $-1.67\beta^* k_B T$ when $L^* = 8$. Therefore, if the system size is small, the infinite loop is highly favorable. According to Ref. [22], long chains start to dominate the system from $\rho^* \geq 0.01$ at $T^* = 0.13$, because rings can easily be broken up through interactions with other particles with increasing density. When 8 particles are present in the system at $L^* = 8$, the density already equals $\rho^* = 0.0156$. Then, an infinite chain formation is more favorable than a ring configuration. Thus, this density distribution gap is not any indication of phase separation but just a finite-size effect. This finite-size effect for the DHS system has been reported only recently [23]. Therefore, I believe that it might affect the simulation results of Ref. [16].

2.3 Specific heat

In the grand-canonical ensemble, the heat capacity is obtained from [24]

$$C_V = \left(\frac{\partial U}{\partial T}\right)_V \tag{2.9}$$

$$= \frac{1}{k_B T^2}\left(\{\langle U^2\rangle - \langle U\rangle^2\} - \left\{\frac{(\langle \rho U\rangle - \langle\rho\rangle\langle U\rangle)^2}{\langle\rho^2\rangle - \langle\rho\rangle^2}\right\}\right). \tag{2.10}$$

The specific heat, $C_V/(Nk_B)$, of the DHS is plotted along an isochore for a wide range of temperatures, $0.11 \leq T^* \leq 0.5$ in Fig. 2.2. Figures 2.2 (a) and (b) represent the specific heat curve for the densities $\rho^* = 0.05$ and 0.10, respectively. It is known that the heat capacity curve shows a divergence at the critical temperature and a discontinuity at the transition temperature if phase separation happens [25]. Simulation results of ionic fluids showed that the height of maximum of the specific heat diverges and that the position of this maximum shifts to the critical temperature at critical density with increasing system size [26]. However, such a size dependence is not observed for the DHS fluid. The specific heat converges for different system sizes for all simulated temperatures as shown in Fig. 2.2.

Figure 2.3(a) shows the specific heat of the DHS as a function of density at $T^* = 0.14$ for three different system sizes. Although it is reported in Ref. [16] that possible phase transitions occur at

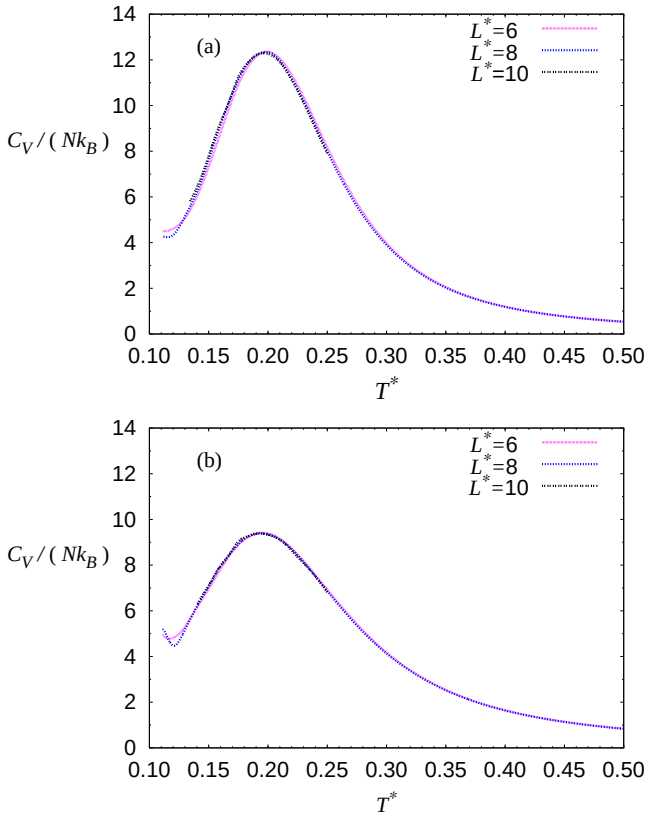

Figure 2.2: The specific heat, C_V/Nk_B, of the DHS as a function of T^* at constant density. Simulations are performed for a range of temperatures, $0.11 \leq T^* \leq 0.5$ for three different system sizes. The heat capacity is calculated by histogram reweighting. (a) $\rho^* = 0.05$. (b) $\rho^* = 0.10$.

densities 0.072 ± 0.008, 0.17 ± 0.02, and 0.28 ± 0.04, the specific heat curves are flat and smooth near those three densities as well as for a wide range of densities, $0.05 \leq \rho^* \leq 0.30$. There is no divergence or system size-dependent maximum. Interestingly, the specific heat curves show a peak at very low density. Figure 2.3(b) enlarges Fig. 2.3(a) for densities below $\rho^* = 0.005$. It is seen that the height of the peak saturates when the system size is larger than $L^* = 8$. Similar behavior is found for $T^* = 0.18$, as shown in Fig. 2.4. In Ref. [11], the possibility of phase separation at $T^* = 0.18$ has already been excluded in the basis of NPT simulations. The specific heat curve at $T^* = 0.18$ still has a peak at very low-density regime and curves coincide in the density range $\rho^* \geq 0.01$. The height of this peak clearly decreases with increasing system size. Since both the specific heat of $T^* = 0.14$ and $T^* = 0.18$ have maxima but do not diverge, these peaks in the specific heat do not represent any evidence of phase transitions but arise from finite-size effects. Therefore, I conclude that there is no phase separation in a range $0.11 \leq T^* \leq 0.5$, despite the estimates of Camp *et al.* [16, 22] for the critical density and temperature, $\rho_c^* \simeq 0.10$ and $T_c^* = 0.15$–0.16.

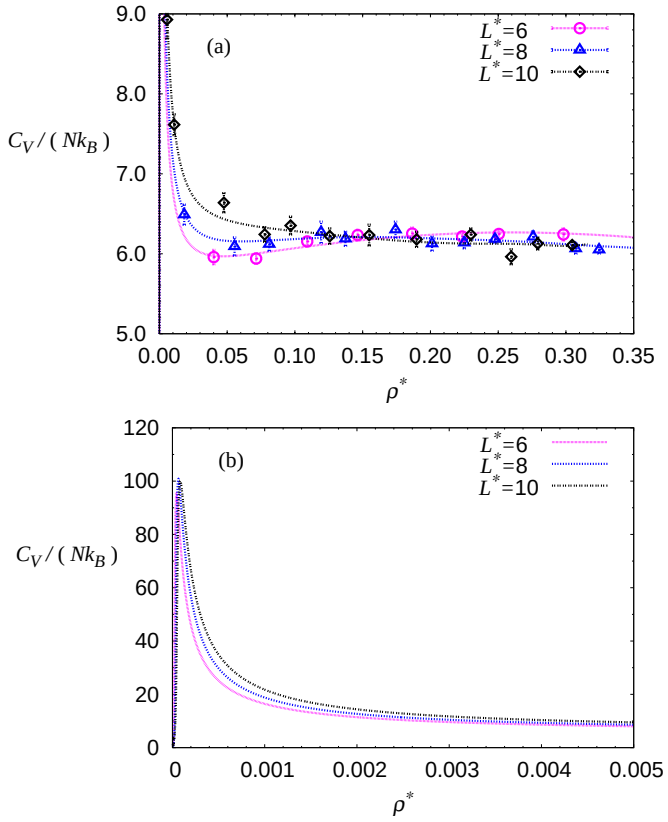

Figure 2.3: (a) The specific heat of the DHS along the $T^* = 0.14$ isotherm for $0 \leq \rho^* \leq 0.35$. System sizes $L^* = 6, 8, 10$ are marked as circles, triangles and diamonds, respectively. Points and error bars indicate the results from GCMC simulations and lines are calculated by histogram reweighting. (b) The isothermal specific heat of the DHS fluids at densities $\rho^* \leq 0.005$.

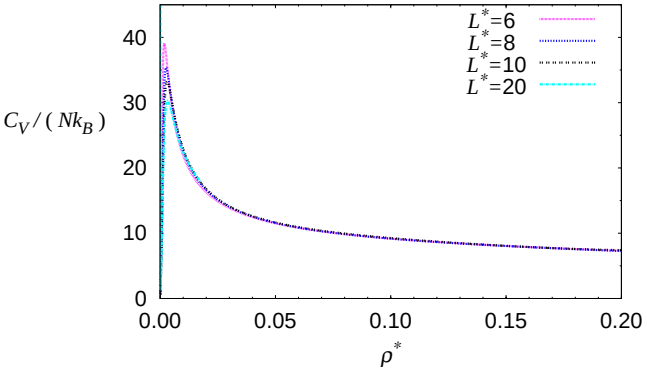

Figure 2.4: The specific heat of the DHS along $T^* = 0.18$ isotherm for $\rho^* \leq 0.20$. System size L^* varies from 6 to 20.

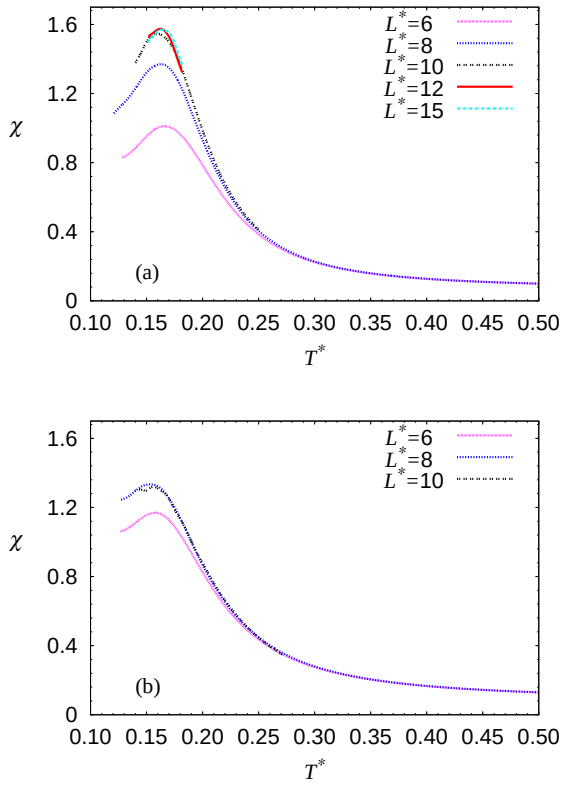

Figure 2.5: The compressibility, χ, of the DHS as a function of T^* at constant density. Simulations are performed for a range of temperatures $0.11 \leq T^* \leq 0.5$. The compressibility is calculated by histogram reweighting. (a) $\rho^* = 0.10$. (b) $\rho^* = 0.15$.

2.4 Compressibility

The compressibility, χ, of the DHS fluid is calculated at constant density for $0.11 \leq T^* \leq 0.5$ in this section. The compressibility is derived from

$$\chi = V\langle(\rho - \langle\rho\rangle)^2\rangle = k_B T \rho^2 K_T \,, \tag{2.11}$$

where K_T is the isothermal compressibility [27, 28]. Figure 2.5 represents the compressibility for the densities $\rho^* = 0.10$ and 0.15, respectively. Unlike the results of the heat capacity, the height of the peaks shows a divergence with increasing system size for the smallest system sizes, which could suggest phase separation. However, ultimately, they converge at larger system size. I find that the peak in the compressibility curve converges at smaller system sizes in the high-density region and shows a stronger divergence in the low-density region. One could argue that this is consistent with the occurrence of phase separation in the low-density system, because finite-size effects become

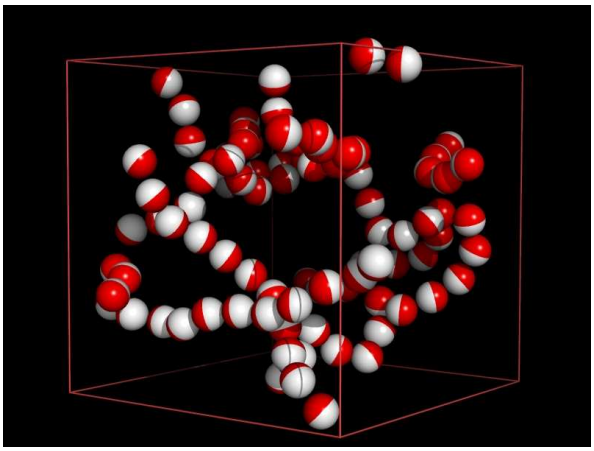

Figure 2.6: The head-to-tail conformation of the dipoles at $T^* = 0.14$ and $\rho^* = 0.09$. One can see several chains in this snapshot. At this low temperature, the dipoles tend to form chain conformations and simulations require a very long time due to the low acceptance rate.

stronger when the system approaches the critical density. However, in Fig. 2.1(c), there is only one peak in the density distribution for this low-density region, which indicates no evidence for the phase transition.

This phenomenon can again be explained from the density distribution gap. Since the density gap effect becomes more severe when the density is low, Fig. 2.5 shows a stronger divergence at low-density regime. On the other hand, the distribution shows no gap at $L^* = 8$ when the average density is larger than $\rho^* \approx 0.15$ as shown in Fig. 2.1, and the compressibility for $\rho^* = 0.15$ indeed converges when the system size is larger than $L^* = 8$. Therefore, I conclude that the divergence in the compressibility appears only when the gap affects the data and does not indicate phase separation.

2.5 Structure

The self-assembled structure of dipolar fluids is quantitatively analyzed in this section. Unlike isotropic ionic interactions, anisotropic dipolar interactions induce head-to-tail conformations at low temperature as can be seen in Fig. 2.6. The classification of clusters, illustrated in Fig. 2.7, proceeds as follows [12, 29]. The first, second, and third nearest-neighbor distances (respectively, r_{1j}, r_{2j}, and r_{3j}) of each particle j are calculated; if $r_{1j} > r_c$, j is a free particle, if $r_{1j} < r_c$ and $r_{2j} > r_c$, j is an end particle, if $r_{2j} < r_c$ and $r_{3j} > r_c$, then j is an interior particle, and, finally, if $r_{3j} < r_c$, j is a junction particle. A ring is defined as a cluster with interior particles only, a chain

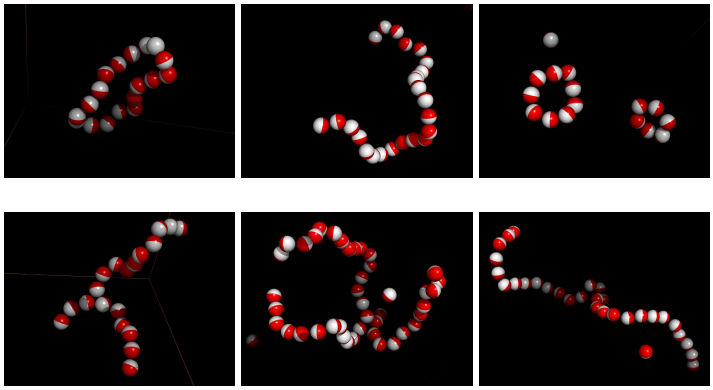

Figure 2.7: Various conformations in the DHS system at low temperature. Chains, rings and networks of various sizes are observed.

is a cluster with two ends, and a network has at least one junction particle. In this study, the cutoff distance is defined as $r_c = 1.125\sigma$ [30].

Figure 2.8(a) shows the fraction of particles belonging to chains, rings, networks and infinite loops as a function of temperature and at the density $\rho^* = 0.10$. With decreasing temperature, the number of monomers decreases monotonically and the numbers of both chain particles and network particles increase as the dipolar attraction increases. Interestingly, upon further decrease of the temperature, chains show a maximum and merge into large networks. Figure 2.8(b) shows that, at the lower density of $\rho^* = 0.01$, chain conformation is always more favorable than network formation even in the low-temperature region. For this low-density system, the rapidly increasing number of infinite chains corresponds to the density gap. The fraction of particles belonging to each cluster is plotted as a function of density at temperatures $T^* = 0.14$ and $T^* = 0.30$ in Fig. 2.9. At $T^* = 0.30$, most of the particles remain isolated since the dipolar interactions are relatively weak at this high temperature. For $\rho^* > 0.08$, the fraction of chains is comparable to the fraction of monomers; however, chains are not long, and are typically just pairs of dipoles. At $T^* = 0.14$, chains dominate the system in the low-density regime, and merge into a network structure as the density is increased. Since most theoretical studies [6–8] only take into account chains and rings, a new theory that includes the effect of network structures is clearly needed.

Since anisotropic dipolar interactions lead to polymer-like chain structures, living polymer theory [31–34] is often used to explain the behavior of dipolar fluids [8,29,35], and the polymerization transition is used to understand self-assembly in systems such as the Stockmayer fluid [35], the quasi

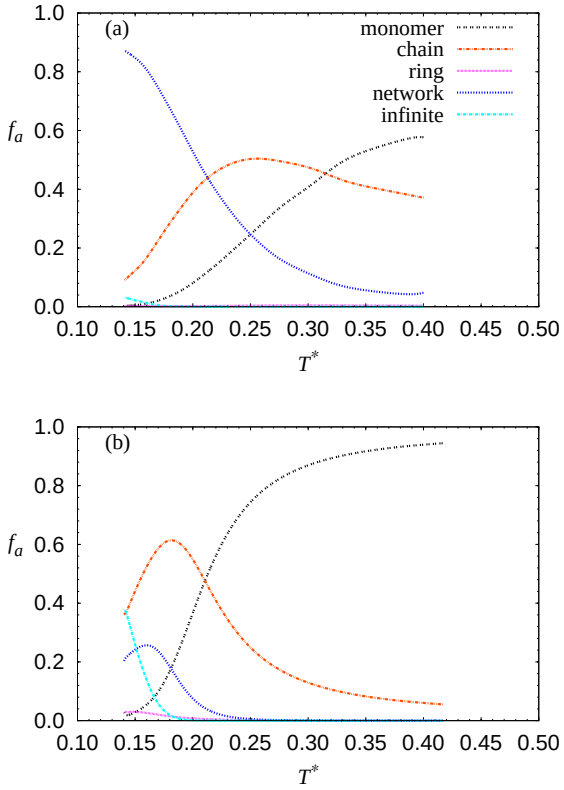

Figure 2.8: (a) Fraction of particles belonging to monomers, chains, rings, networks and infinite loops. Properties are measured as a function of temperature at constant density $\rho^* = 0.10$ and $L^* = 10$. Black, orange, pink, blue and cyan color correspond to monomer, chain, ring, network, and infinite loop, respectively. (b) Same figure at constant density $\rho^* = 0.01$.

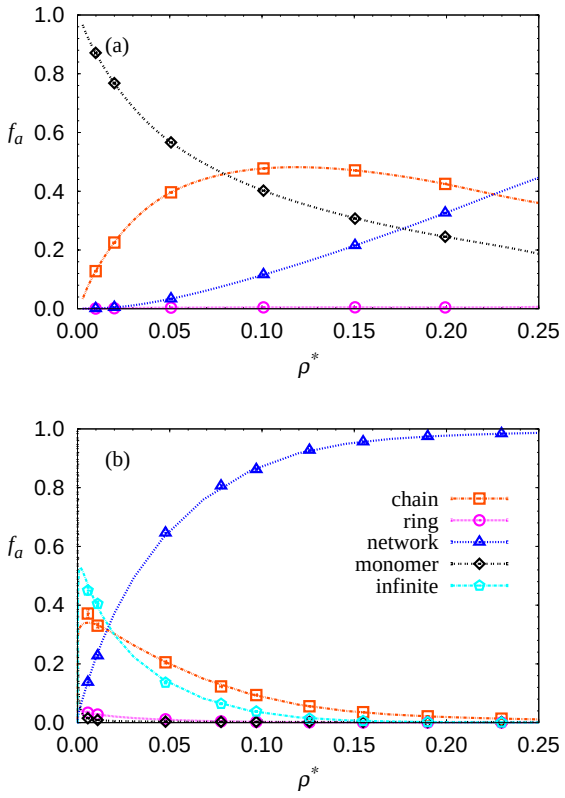

Figure 2.9: (a) Fraction of dipolar particles belonging to monomers, chains, rings, networks and infinite loops. Properties are measured as a function of density at constant temperature $T^* = 0.30$ and $L^* = 10$. Black, orange, pink, blue and cyan color correspond to monomer, chain, ring, network, and infinite loop structure, respectively. (b) Same figure at constant temperature $T^* = 0.14$.

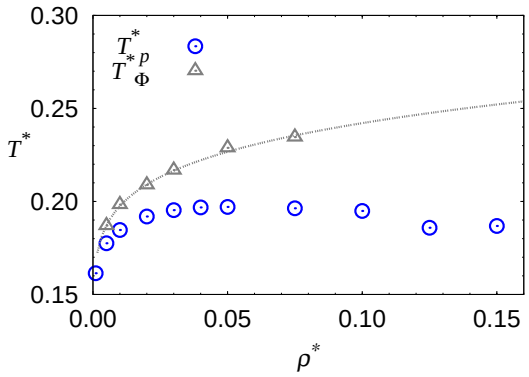

Figure 2.10: Circles are the polymerization transition temperatures calculated from the maximum in the heat capacity. Triangles indicate the polymerization temperatures from the inflection point of the extent of polymerization and a dotted gray line is a fitting line.

two-dimensional DHS [30], as well as polymer systems [36]. However, it has not been applied in the 3D DHS system. The polymerization transition is defined in two different ways [34–36]. One way to define the polymerization transition temperature, T_p^*, is to identify it with the peak of the heat capacity. Figure 2.10 shows simulation results for the DHS system. T_p^* increases when $\rho^* \leq 0.05$ and decreases at higher densities. For the Stockmayer fluid, increasing behavior of T_p^* at low densities ($\rho^* \leq 0.0637$) are also observed [35]. The second way to define the polymerization transition line is through the extent of polymerization, $\Phi = N_p/N$, where N_p is the number of aggregated particles. Here, the polymerization temperature, T_Φ^*, is defined as the inflection point $(\partial^2\Phi/\partial T^{*2})\ |_\rho = 0$. Below this temperature, the average chain length in the system becomes roughly longer than 2. In Fig. 2.10, T_Φ^* always appears above T_p^*, consistent with simulation results for the Stockmayer fluid [35].

2.6 Summary and conclusions

The heat capacity, compressibility, and density distribution have been calculated for the DHS system to investigate the possibility of phase separation using GCMC simulations. I simulate this system for temperatures as low as $T^* = 0.11$, despite the long equilibration times associated with the low acceptance rate. The density distribution displays only a single peak at each chemical potential, suggesting that there is no phase separation. In addition, my calculation of the heat capacity and compressibility does not indicate any evidence for phase separation.

Interestingly, recent simulation studies used extrapolation from other system to estimate the critical temperature of the DHS fluid [23, 37]. Both references estimated the critical temperature at $T_c^* \approx 0.15$, supporting simulation data of Camp *et al.* [16]. Ganzenmüller and Camp simulated a fluid of charged hard dumbbells (CHD), where each dumbbell is composed of two oppositely charged hard spheres at a center–center distance d [23]. When $d/\sigma = 1$, the CHD shows ionic phase separation. As $d/\sigma \to 0$, the CHD system becomes the DHS system. They found that the critical temperature increases with decreasing a center–center distance d and extrapolated the critical temperature of the DHS system. Almarza *et al.* simulated mixtures of hard spheres and dipolar hard spheres [37]. When the pressure of this mixture is decreased, the hard-sphere density decreases and this mixture becomes a pure DHS system. Since they found the critical temperatures of this mixtures at different pressures, they could extrapolate the critical temperature of the DHS system. However, both Refs. [23,37] did not have simulation data for the pure DHS system. Therefore, these extrapolation methods does not guarantee the existence of phase separation in the DHS system. My simulation results of the DHS system clearly exclude the occurrence of phase separation for a large region of the temperature–density plane, and if phase separation happens, it would be below $T^* = 0.11$.

2.7 References

[1] P. G. de Gennes and P. A. Pincus, "Pair correlations in a ferromagnetic colloid," Phys. Kondens. Mater. **11**, 189–198 (1970).

[2] M. S. Wertheim, "Exact solution of the mean spherical model for fluids of hard spheres with permanent electric dipole moments," J. Chem. Phys. **55**, 4291–4298 (1971).

[3] G. S. Rushbrooke, G. Stell and J. S. Høye, "Theory of polar liquids, I. Dipolar hard spheres," Mol. Phys. **26**, 1199–1215 (1973).

[4] V. I. Kalikmanov, "Statistical thermodynamics of ferrofluids," Physica A **183**, 25–50 (1992).

[5] T. Tlusty and S. A. Safran, "Defect-induced phase separation in dipolar fluids," Science **290**, 1328–1331 (2000).

[6] R. P. Sear, "Low-density fluid phase of dipolar hard spheres," Phys. Rev. Lett. **76**, 2310–2313 (1996).

[7] R. van Roij, “Theory of chain association versus liquid condensation,” Phys. Rev. Lett. **76**, 3348–3351 (1996).

[8] J. M. Tavares, M. M. Telo da Gama and M. A. Osipov, “Criticality of dipolar fluids: Liquid-vapor condensation versus phase separation in systems of living polymers,” Phys. Rev. E **56**, R6252–R6255 (1997).

[9] Y. Levin, “What happened to the gas-liquid transition in the system of dipolar hard spheres?,” Phys. Rev. Lett. **83**, 1159–1162 (1999).

[10] K.-C. Ng, J. P. Valleau, G. M. Torrie and G. N. Patey, “Liquid–vapour co-existence of dipolar hard spheres,” Mol. Phys. **38**, 781–788 (1979).

[11] J.-M. Caillol, “Search of the gas–liquid transition of dipolar hard spheres,” J. Chem. Phys. **98**, 9835–9849 (1993).

[12] J. J. Weis and D. Levesque, “Chain formation in low density dipolar hard spheres: A Monte Carlo study,” Phys. Rev. Lett. **71**, 2729–2732 (1993).

[13] M. E. van Leeuwen and B. Smit, “What makes a polar liquid a liquid?,” Phys. Rev. Lett. **71**, 3991–3994 (1993).

[14] S. C. McGrother and G. Jackson, “Island of vapor-liquid coexistence in dipolar hard-core systems,” Phys. Rev. Lett. **76**, 4183–4186 (1996).

[15] J. C. Shelley, G. N. Patey, D. Levesque and J. J. Weis, “Liquid-vapor coexistence in fluids of dipolar hard dumbbells and spherocylinders,” Phys. Rev. E **59**, 3065–3070 (1999).

[16] P. J. Camp, J. C. Shelley and G. N. Patey, “Isotropic fluid phases of dipolar hard spheres,” Phys. Rev. Lett. **84**, 115–118 (2000).

[17] S. W. de Leeuw, J. W. Perram and E. R. Smith, “Simulation of electrostatic systems in periodic boundary conditions. I. Lattice sums and dielectric constants,” Proc. R. Soc. London, Ser. A **373**, 27–56 (1980).

[18] D. Frenkel and B. Smit, *Understanding Molecular Simulation*, 2nd ed. (Academic, San Diego, 2002).

[19] B. Widom, “Some topics in the theory of fluids,” J. Chem. Phys. **39**, 2808–2812 (1963).

[20] Y. Miyatake, M. Yamamoto, J. J. Kim, M. Toyonaga and O. Nagai, “On the implementation of the ‘heat bath’ algorithms for Monte Carlo simulations of classical Heisenberg spin systems,” J. Phys. C **19**, 2539–2545 (1986).

[21] A. M. Ferrenberg and R. H. Swendsen, "New monte carlo technique for studying phase transition," Phys. Rev. Lett. **61**, 2635–2638 (1988).

[22] P. J. Camp and G. N. Patey, "Structure and scattering in colloidal ferrofluids," Phys. Rev. E **62**, 5403–5408 (2000).

[23] G. Ganzenmüller and P. J. Camp, "Vapor-liquid coexistence in fluids of charged hard dumbbells," J. Chem. Phys. **126**, 191104 (2007).

[24] J. L. Lebowitz, J. K. Percus and L. Verlet, "Ensemble dependence of fluctuations with application to machine computations," Phys. Rev. **153**, 250–254 (1967).

[25] H. E. Stanley, *Introduction to Phase Transitions and Critical Phenomena* (Oxford University Press, Oxford, 1971).

[26] E. Luijten, M. E. Fisher and A. Z. Panagiotopoulos, "The heat capacity of the restricted primitive model electrolyte," J. Chem. Phys. **114**, 5468–5471 (2001).

[27] G. Orkoulas, M. E. Fisher and A. Z. Panagiotopoulos, "Precise simulation of criticality in asymmetric fluids," Phys. Rev. E **63**, 051507 (2001).

[28] E. Luijten, M. E. Fisher and A. Z. Panagiotopoulos, "Universality class of criticality in the restricted primitive model electrolyte," Phys. Rev. Lett. **88**, 185701 (2002).

[29] J. M. Tavares, J. J. Weis and M. M. Telo da Gama, "Quasi-two-dimensional dipolar fluid at low densities: Monte Carlo simulations and theory," Phys. Rev. E **65**, 061201 (2002).

[30] J. Stambaugh, K. K. van Workum, J. F. Douglas and W. Losert, "Polymerization transitions in two-dimensional systems of dipolar spheres," Phys. Rev. E **72**, 031301 (2005).

[31] J. Dudowicz, K. F. Freed and J. F. Douglas, "Lattice model of living polymerization. I. Basic thermodynamic properties," J. Chem. Phys. **111**, 7116–7130 (1999).

[32] J. Dudowicz, K. F. Freed and J. F. Douglas, "Lattice model of living polymerization. II. Interplay between polymerization and phase stability," J. Chem. Phys. **112**, 1002–1010 (2000).

[33] J. Dudowicz, K. F. Freed and J. F. Douglas, "Lattice model of living polymerization. III. Evidence for particle clustering from phase separation properties and," J. Chem. Phys. **113**, 434–446 (2000).

[34] J. Dudowicz, K. F. Freed and J. F. Douglas, "Lattice model of equilibrium polymerization. IV. Influence of activation, chemical initiation, chain scission and fusion, and chain stiffness on polymerization and phase separation," J. Chem. Phys. **119**, 12645–12666 (2003).

[35] K. van Workum and J. F. Douglas, “Equilibrium polymerization in the Stockmayer fluid as a model of supermolecular self-organization,” Phys. Rev. E **71**, 031502 (2005).

[36] S. C. Greer, “Physical chemistry of equilibrium polymerizations,” J. Phys. Chem. B **102**, 5413–5422 (1998).

[37] N. G. Almarza, E. Lomba, C. Martín and A. Gallardo, “Demixing in binary mixtures of apolar and dipolar hard spheres,” J. Chem. Phys. **129**, 234504 (2008).

CHAPTER 3

QUASI-2-DIMENSIONAL DIPOLAR HARD-SPHERE FLUID

A recent experiment on dipolar colloids confined to a plane showed interesting stripe patterns induced by phase separation [1]. A simulation study of 2D dipolar fluids can be a potential starting point to understand this experimental result. Furthermore, it is well established that Coulombic interactions in different dimensions can induce different types of phase separation [2–9]; it is a fundamental question to understand the phase behavior of dipolar fluids in different dimensions. The simulation results of the previous Chapter for the 3D dipolar hard-sphere (DHS) system exclude the possibility of liquid–vapor phase separation for a large region of the temperature–density plane. Next interesting DHS system with different dimensionality would be a quasi-2D DHS fluid because the dipole moment can rotate in full 3D space like for the 3D DHS model, but the centers of the dipolar spheres are confined to a plane. Thus, how this dimensional restriction changes the phase behavior of DHS fluids is a fundamentally interesting question. Since the occurrence of phase separation in the quasi-2D DHS fluid is still an open question [10–16], I investigate this in this Chapter.

3.1 Simulation methodology

To study the quasi-2D DHS model, I use the same simulation methodology as described in Chapter 2. Reduced parameters $\rho^* = N\sigma^2/L^2$, T^*, L^*, and μ^* are used in this simulation as in Chapter 2. Ewald summation method is implemented to calculate the long-range dipole-dipole interaction, where the centers of the dipoles are restricted to a plane and the dipole moment vectors are fully 3D [12, 17]. Since the quasi-2D system does not have a periodicity in z direction, now long-range interactions can be separated into an in-plane component and an out-of-plane component. Thus, a different derivation for Ewald summation is necessary for the quasi-2D system [17].

To investigate the possibility of phase separation, I simulate the system over a wide range of temperatures $T^* = 0.1322$–0.50 and densities $0.05 \leq \rho^* \leq 0.20$. Finite-size effects are investigated

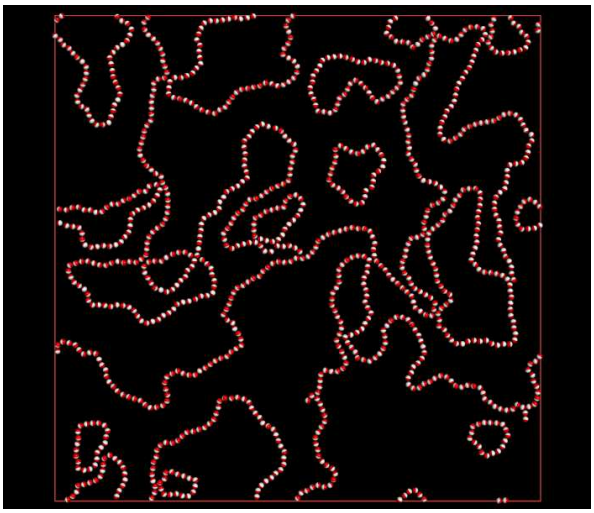

Figure 3.1: Typical conformation of dipolar spheres confined to a plane at $T^* = 0.1322$, $L^* = 80$ and $\rho^* = 0.16$. At low temperature, dipoles form head-to-tail conformations, and ring and network structures are observed in this snapshot.

by varying the system size $L^* = 8$–80. As in Chapter 2, this simulation is performed using a combination of grand-canonical and canonical moves. The orientational-bias method is used to increase efficiency [18, 19].

About 5.0×10^{10} MC steps are needed to equilibrate the system at $T^* = 0.1322$, $\mu^* = -1.3395$ (which corresponds to a planar density $\rho^* \approx 0.093$) and $L^* = 30$, starting from a random initial configuration. To obtain 5000 independent configurations after equilibration, I simulate 5.0×10^{12} MC steps for the same system. The acceptance rate for the GCMC moves is 0.15% and the acceptance rate for the canonical moves is 16.20% for this system. The total CPU time required to obtain all data at $L^* = 30$, $T^* = 0.1322$ is 16 years for a single core of an Intel Xeon EM64T 3.0GHz. In total, I have used $\sim$140 CPU years to perform all simulations for this project. A typical configuration of the quasi-2D DHS fluid at $T^* = 0.1322$ is depicted in Fig. 3.1.

3.2 Thermodynamic properties

In Chapter 2, I have disproved phase separation for the 3D DHS, contradicting the evidence of Camp *et al.* at $T^* = 0.14$ [20]. Interestingly, slightly below this temperature [16], a theoretical estimation of Tavares *et al.* suggested the occurrence of a second-order phase transition of the quasi-2D DHS system at $T^* = 0.1322$ [16]. Therefore, I want to focus on the temperature $T^* = 0.1322$ and $T^* = 0.14$ to investigate the occurrence of a phase transition.

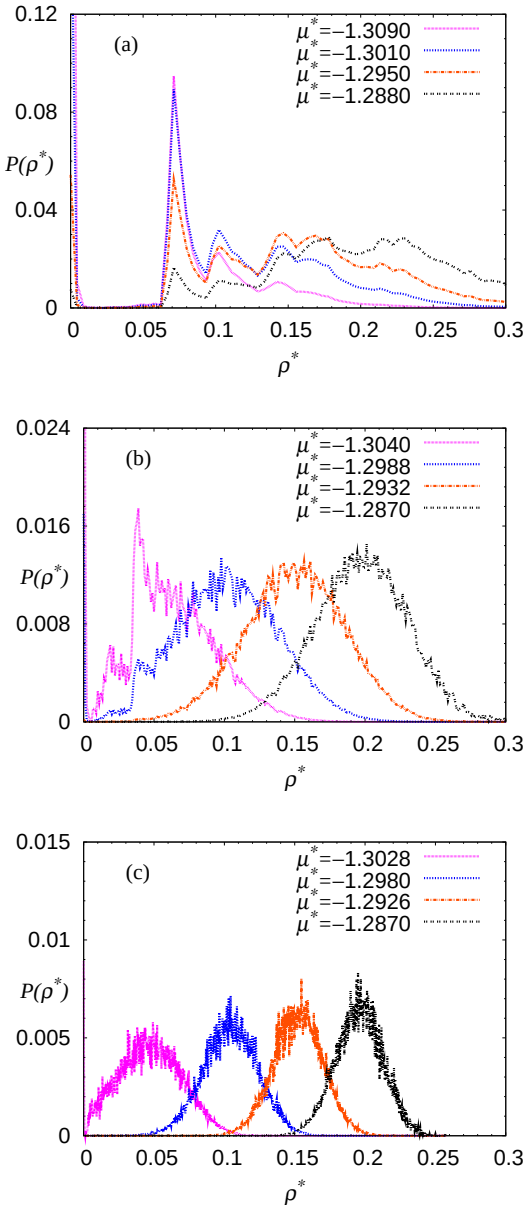

Figure 3.2: Isothermal density distribution of the quasi-2D dipolar fluid at various chemical potentials. (a) $T^* = 0.14$ and $L^* = 15$. The density distributions for the chemical potentials $\mu^* = -1.3090, -1.3010, -1.2950, -1.2880$ correspond to the average densities $\rho^* \approx 0.05, 0.10, 0.15, 0.20$, respectively. (b) $T^* = 0.14$ and $L^* = 30$. The density distributions for $\mu^* = -1.3040, -1.2988, -1.2932, -1.2870$ represent $\rho^* \approx 0.05, 0.10, 0.15, 0.20$, respectively. (c) $T^* = 0.14$ and $L^* = 60$. The density distributions for $\mu^* = -1.3028, -1.2980, -1.2926, -1.2870$ represent $\rho^* \approx 0.05, 0.10, 0.15, 0.20$, respectively.

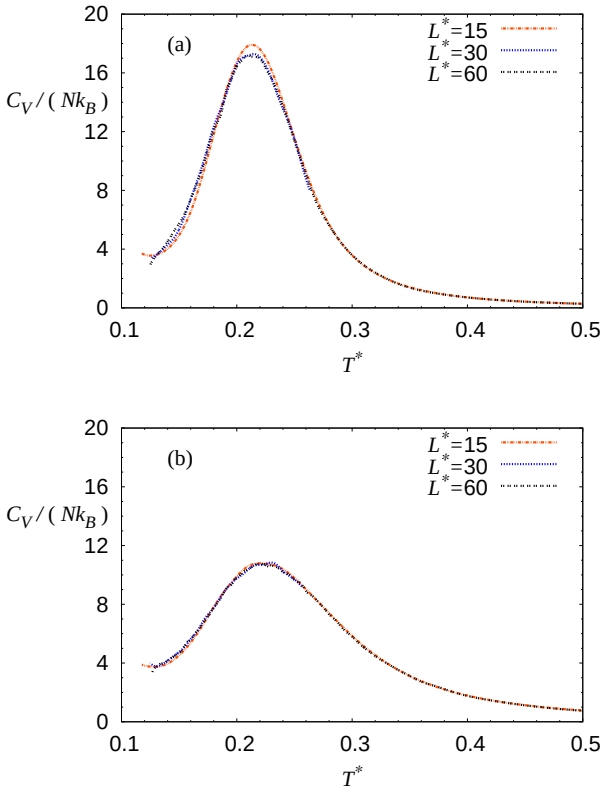

Figure 3.3: Specific heat, C_V/Nk_B, of the quasi-2D DHS as a function of T^* at constant density. Simulations are performed for a range of temperatures, $0.1322 \leq T^* \leq 0.5$ for three different system sizes. The specific heat curves are calculated by histogram reweighting [21]. (a) $\rho^* = 0.05$. (b) $\rho^* = 0.15$.

Figure 3.2 shows the density distributions of the quasi-2D dipolar fluids at $T^* = 0.14$ and various chemical potentials. Similar to Chapter 2, a density gap appears in the density distribution, with a temperature and system-size dependence. The approximate locations of the peaks are $\rho^*_{\text{peak}} \approx 1/L^{*2}$ and $\rho^*_{\text{peak}} \approx 1/L^*$ (which corresponds to a single horizontal or vertical spanning loop) for the 3D and 2D systems, respectively. Thus, the gap in the 2D system is broader than that in 3D at the same system size. At $L^* = 15$, Fig. 3.2(a) shows that a *second* peak arises at $\rho^*_{\text{peak}} \approx \sqrt{2}/L^*$, which corresponds to a single diagonally spanning infinite loop. The gap even affects the distribution of the system at $\mu^* = -1.288$ (which corresponds to an average density $\rho^* \approx 0.20$). In Fig. 3.2(b), the density gap becomes shallower at $L^* = 30$. The gap is only visible for densities lower than $\rho^* \approx 0.10$. Finally, at $L^* = 60$, Fig. 3.2(c) shows that the density gap disappears. Since the density gap effect is severe in 2D, large system size are required to eliminate this finite-size effect, making the total simulation cost comparable to that of the 3D system.

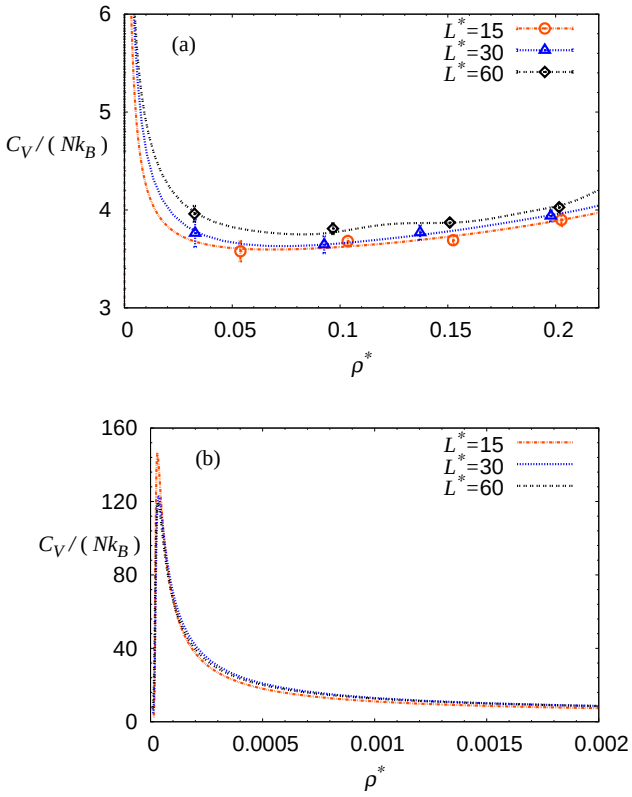

Figure 3.4: (a) Specific heat of the quasi-2D DHS along the $T^* = 0.1322$ isotherm for $0 \leq \rho^* \leq 0.22$. System sizes $L^* = 15, 30, 60$ are marked as circles, triangles and diamonds, respectively. Points and error bars indicate the results from GCMC simulations and lines are calculated by histogram reweighting. (b) Isothermal specific heat of the quasi-2D DHS fluids at densities $\rho^* \leq 0.002$.

At $T^* = 0.14$, the finite-size gap effects are eliminated by choosing $L^* = 60$, and for this system Only a single peak is observed in the density distribution as shown in Fig. 3.2(c), and therefore there is no sign of phase separation. Further simulations indicate that, even at $T^* = 0.1322$, there is a single peak in the density distribution at various chemical potentials that correspond to a wide range of average densities $\rho^* = 0.05$–0.20.

Figures 3.3(a) and (b) show the specific heat, C_V/Nk_B, of the quasi-2D DHS as a function of T^* at densities $\rho^* = 0.05$ and $\rho^* = 0.15$. The specific heat curves for the different system sizes coincide. I study several densities between $0.05 \leq \rho^* \leq 0.20$, and do not observe any evidence for a maximum that diverges with system size or a discontinuity in the specific heat curves. In Fig. 3.3(a), the maximum of the curve for $L^* = 15$ is slightly higher than the maxima of other curves. As shown in the density distribution, the results for $L^* = 15$ are strongly affected by the gap at low density. Therefore, this deviation in the maximum can be interpreted as a finite-size effect.

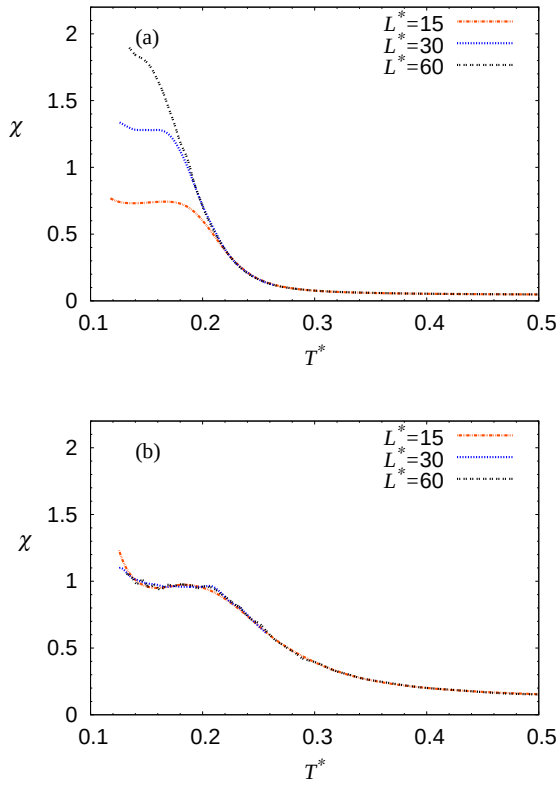

Figure 3.5: Compressibility χ of the quasi-2D DHS as a function of temperature at constant density. Simulations are performed for a range of temperatures $0.1322 \leq T^* \leq 0.5$. (a) $\rho^* = 0.05$. (b) $\rho^* = 0.20$.

I also check the specific heat as a function of density at $T^* = 0.1322$ for three different system sizes in Fig. 3.4. For densities in the range $0.03 \leq \rho^* \leq 0.20$, I do not find any discontinuity and the curves for three different system sizes almost coincide. Like for the 3D DHS system, the specific heat curves of the quasi-2D DHS system also display a peak at very low density. Figure 3.4(b) enlarges this low density regime, confirming that the height of these peaks decreases with increasing system size as observed in the 3D DHS.

Figures 3.5(a) and (b) show the compressibility χ of the quasi-2D DHS system as a function of T^* at densities $\rho^* = 0.05$ and 0.20, respectively. At $\rho^* = 0.05$, the compressibility appears to diverge due to the finite-size density gap effect similar to the 3D case. This divergence disappears when $\rho^* = 0.20$ because the density gap occurs at lower densities. Once the gap effects are removed, the compressibility curves are smooth and converge. Therefore, the compressibility of the quasi-2D DHS system does not indicate any phase separation.

Tavares *et al.* [16] calculated the chemical potential as a function of corresponding density at

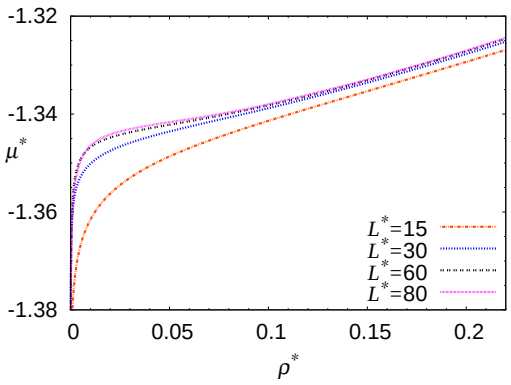

Figure 3.6: Chemical potential as a function of density at $T^* = 0.1322$.

$T^* = 0.1322$, finding a cusp in the curve. Consequently, the second derivative of the free energy, $\left(\frac{\partial \mu}{\partial \rho}\right)_{T^*} \equiv \left(\frac{\partial^2 G}{\partial \rho^2}\right)_{T^*}$ shows a discontinuity at a finite density. Since my simulation is performed in grand-canonical ensemble, the average density at each chemical potential is measured, then chemical potentials and corresponding densities are calculated by histogram reweighting [21] as shown in Fig. 3.6. Curves for small system sizes show a finite-size dependence, but the curves for $L^* = 60$ and $L^* = 80$ coincide almost perfectly and can thus be viewed as representative in the thermodynamic limit. Since no discontinuity is observed in Fig. 3.6, I conclude that theoretical prediction is not reliable in a range of densities $0.05 \leq \rho^* \leq 0.20$ at $T^* = 0.1322$.

3.3 Summary and conclusions

I have excluded the possibility of phase separation in the 3D DHS system in the previous Chapter. How dimensionality affects the phase behavior of dipolar fluids is a fundamentally important question. Interestingly, furthermore, theoretical prediction has shown the possibility of a second-order phase transition in the quasi-2D DHS system at $T^* = 0.1322$ [16]. In this Chapter, I have investigated the possibility of phase separation in the quasi-2D DHS system. I have performed simulations for a large temperature–density region, and calculated the density distribution, heat capacity, and compressibility. The behavior of those properties is comparable to their counterparts in the 3D DHS system, and I do not find any evidence of phase separation in the quasi-2D DHS system. Despite the theoretical prediction of a phase transition, I exclude this for temperatures as low as $T^* = 0.1322$. At this temperature, the binding energy of a head-to-tail conformation is around $-15 k_B T$. Thus,

if this strong chain formation preempts the existence phase separation, it is plausible that phase separation can not be occurred below this temperature because of more strongly bonded chains.

3.4 References

[1] A. Ghezelbash, B. Koo and B. A. Korgel, "Self-assembled stripe patterns of CdS nanorods," Nano Letters **6**, 1832–1836 (2006).

[2] G. Orkoulas and A. Z. Panagiotopoulos, "Free energy and phase equilibria for the restricted primitive model of ionic fluids from Monte Carlo simulations," J. Chem. Phys. **101**, 1452–1459 (1994).

[3] E. Luijten, M. E. Fisher and A. Z. Panagiotopoulos, "The heat capacity of the restricted primitive model electrolyte," J. Chem. Phys. **114**, 5468–5471 (2001).

[4] E. Luijten, M. E. Fisher and A. Z. Panagiotopoulos, "Universality class of criticality in the restricted primitive model electrolyte," Phys. Rev. Lett. **88**, 185701 (2002).

[5] J. J. Weis, D. Levesque and J. M. Caillol, "Restricted primitive model of an ionic solution confined to a plane," J. Chem. Phys. **109**, 7486–7496 (1998).

[6] G. Orkoulas and A. Z. Panagiotopoulos, "Phase diagram of the two-dimensional Coulomb gas: A thermodynamic scaling Monte Carlo study," J. Chem. Phys. **104**, 7205–7209 (1996).

[7] J. Lidmar and M. Wallin, "Monte Carlo simulation of a two-dimensional continuum Coulomb gas," Phys. Rev. B **55**, 522–530 (1997).

[8] E. Lomba, J. J. Weis and F. Lado, "Structure and thermodynamics of a two-dimensional Coulomb fluid in the strong association regime," J. Chem. Phys. **127**, 074501 (2007).

[9] A. R. Mehrabi and M. Sahimi, "Cluster conformations and multipole distributions in ionic fluids. I. Two-dimensional systems of mobile ions," J. Chem. Phys. **128**, 234503 (2008).

[10] J. J. Weis, "Orientational structure of quasi-two-dimensional dipolar hard spheres," Mol. Phys. **93**, 361–364 (1998).

[11] S. Davis, H. C. M. W. McCausland, C. T. Tanaka and M. Widom, "Cluster-based Monte carlo simulation of ferrofluids," Phys. Rev. E **59**, 2424–2428 (1999).

[12] E. Lomba, F. Lado and J. J. Weis, "Structure and thermodynamics of a ferrofluid monolayer," Phys. Rev. E **61**, 3838–3849 (2000).

[13] J. J. Weis, “Orientational structure in a monolayer of dipolar hard spheres,” Mol. Phys. **100**, 579–594 (2002).

[14] J. M. Tavares, J. J. Weis and M. M. Telo da Gama, “Quasi-two-dimensional dipolar fluid at low densities: Monte Carlo simulations and theory,” Phys. Rev. E **65**, 061201 (2002).

[15] J. Stambaugh, K. K. van Workum, J. F. Douglas and W. Losert, “Polymerization transitions in two-dimensional systems of dipolar spheres,” Phys. Rev. E **72**, 031301 (2005).

[16] J. M. Tavares, J. J. Weis and M. M. Telo da Gama, “Phase transition in two-dimensional dipolar fluids at low densities,” Phys. Rev. E **73**, 041507 (2006).

[17] G. T. Gao, X. C. Zeng and W. Wang, “Vapor–liquid coexistence of quasi-two-dimensional Stockmayer fluids,” J. Chem. Phys. **106**, 3311–3317 (1996).

[18] Y. Miyatake, M. Yamamoto, J. J. Kim, M. Toyonaga and O. Nagai, “On the implementation of the ‘heat bath’ algorithms for Monte Carlo simulations of classical Heisenberg spin systems,” J. Phys. C **19**, 2539–2545 (1986).

[19] J.-M. Caillol, “Search of the gas–liquid transition of dipolar hard spheres,” J. Chem. Phys. **98**, 9835–9849 (1993).

[20] P. J. Camp, J. C. Shelley and G. N. Patey, “Isotropic fluid phases of dipolar hard spheres,” Phys. Rev. Lett. **84**, 115–118 (2000).

[21] A. M. Ferrenberg and R. H. Swendsen, “New monte carlo technique for studying phase transition,” Phys. Rev. Lett. **61**, 2635–2638 (1988).

CHAPTER 4

ION–DIPOLE MIXTURES

The phase behavior of binary van der Waals mixtures has been studied theoretically and experimentally, and a classification of phase diagrams has been established [1–5]. However, our knowledge of phase behavior driven by *electrostatic* interactions is far from complete. While it is known that Coulombic interactions can induce phase separation [6, 7], I have excluded the possibility of fluid–fluid phase separation in purely dipolar fluids in Chapter 2. The next natural question is whether phase separation takes place in mixtures that contain ions as well as dipolar particles. Theoretical studies for ion–dipole mixtures are not reliable since they start from the assumption that dipoles have a liquid–gas phase transition [8–10]. Previous simulation studies [11–15] for ion–dipole mixtures were performed for high dipole densities and weak dipolar interactions, and only focused on structural information. In this Chapter, I present results for a broad range of dipole and ion densities using various dipolar to ionic interaction ratios. I map out the phase diagrams of these mixtures and locate their critical points.

4.1 Simulation methodology

To study ion–dipole binary mixtures, I use a combination of the dipolar hard sphere (DHS) and the restricted primitive model (RPM) to model the dipoles and ions, respectively. The DHS is described in Chapter 2, and the RPM represents ions as hard spheres with equal diameter that carry a positive or negative charge of identical magnitude. The system is charge neutral. The pair potential between charged particles is

$$U_{ij}^{qq} = U_{\mathrm{HS}}(r_{ij}) + \frac{q_i q_j}{4\pi\varepsilon_0\varepsilon r_{ij}}\,, \tag{4.1}$$

and the pair potential between a charge and a dipole is

$$U_{ij}^{qp} = U_{\mathrm{HS}}(r_{ij}) + \frac{q_i\, p(\hat{\boldsymbol{p}}_j \cdot \hat{\boldsymbol{r}}_{ij})}{4\pi\varepsilon_0\varepsilon r_{ij}^2}\,. \tag{4.2}$$

where $U_{\mathrm{HS}}(r_{ij})$ is the hard-sphere interaction, ε is the dielectric constant of the medium, ε_0 is the dielectric permeability of the vacuum, q_i is the charge of ion i, p is the dipole moment, $\hat{\boldsymbol{p}}_i$ is the unit vector indicating the dipole orientation of particle i, $\hat{\boldsymbol{r}}_{ij}$ is the unit vector along the interparticle vector $\boldsymbol{r}_{ij}$, and r_{ij} is its magnitude. I use reduced properties in this study, i.e., I define the reduced total density $\rho^*_{\mathrm{total}} = N\sigma^3/V$, the reduced ionic density $\rho^*_{\mathrm{ion}} = N_{\mathrm{ion}}\sigma^3/V$, the reduced dipolar density $\rho^*_{\mathrm{dipole}} = N_{\mathrm{dipole}}\sigma^3/V$, the reduced temperature $T^* = 4\pi\varepsilon_0\varepsilon\sigma k_B T/q^2$, the reciprocal temperature $\beta^* = 1/T^*$, the reduced dipole moment $p^* = p/(q\sigma)$, the reduced chemical potential $\mu^* = \mu T^*/(k_B T)$, and the reduced system size $L^* = L/\sigma$, where N is the total number of spheres in the system, N_{ion} is the sum of the number of positive and negative ions, N_{dipole} is the number of dipoles, σ is the diameter of a dipole or ion, V is the volume of the system, and k_B is Boltzmann's constant. The dipole moment in this Chapter is related to the dipolar temperature used in Chapter 2 as $T^*_{\mathrm{DHS}} = T^*/p^{*2}$. Ewald summation is employed for the calculation of long-range dipolar, ionic and ion–dipole interactions with periodic boundary conditions [16, 17].

To study these binary systems, I focus on the reciprocal temperature $\beta^* = 21.0$ ($T^* = 0.04762$), where Coulombic interactions are strong enough to induce a liquid–gas phase transition [6, 7]. My goal in this Chapter is to investigate the phase behavior of mixtures when dipoles are added to ionic fluids. Certainly, the interaction between ions and dipoles will affect the phase behavior of such ion–dipole mixtures. Thus, to change the ion–dipole interactions, the dipole moment is varied in the range $p^* = 0$–0.60. At $p^* = 0$, "dipoles" become hard spheres without any additional interactions. The dipolar temperature is $T^*_{\mathrm{DHS}} = 0.132$ when $p^* = 0.60$. As explained in Chapter 2, dipoles form strong head-to-tail conformation at this dipolar temperature. Since this is a binary mixture, both the chemical potentials μ^*_{dipole} and μ^*_{ion} need to be tuned. To find phase coexistence, I first find the ionic chemical potential μ^*_{ion} that leads to phase separation in pure ionic fluids. Then, a reasonable μ^*_{dipole}, that results in a small amount of dipoles in the system, is also found from simulations. Subsequently, μ^*_{dipole} is kept fixed, and μ^*_{ion} is varied, and each set of chemical potentials produces an average ion composition $x_{\mathrm{ion}} = N_{\mathrm{ion}}/(N_{\mathrm{ion}} + N_{\mathrm{dipole}})$. The occurrence of phase separation is

determined by calculating the density distribution of each system. Once the existence of phase separation is determined at fixed $\mu^*_{\rm dipole}$, $\mu^*_{\rm dipole}$ is increased to increase the amount of dipoles and $\mu^*_{\rm ion}$ is varied again. Thus, the phase diagram is mapped out. The correspondence between the chosen chemical potentials and the actually measured densities is checked via the Widom insertion method [16, 18]. I use system sizes in the range $L^* = 8$–15 to explore finite-size effects.

As in Chapter 2, this simulation is performed using a combination of grand-canonical and canonical moves. To maintain charge neutrality in this mixture, a positive ion and negative ion are inserted or deleted together. At low temperature, most of the ions are found as neutral 1–1 pairs, and it is energetically cost to break such ionic pairs. To maintain a reasonable acceptance rate for ionic moves, the distance bias method [6] is implemented. For dipolar moves, I use the orientational-bias method described in Chapter 2. Typically, 7.5×10^{10} Monte Carlo (MC) steps are needed to equilibrate the system at $T^* = 0.04762$, $p^* = 0.60$, $\mu^*_{\rm dipole} = -0.5044$, $\mu^*_{\rm ion} = -1.3534$ (which correspond to densities $\rho^*_{\rm dipole} \approx 0.07$, $\rho^*_{\rm ion} \approx 0.04$), and $L^* = 12$. To obtain 10000 independent configurations after equilibration, I simulate 1.5×10^{12} MC steps for the same system. For this system, the acceptance rate for GCMC moves of ionic pairs is 8.6%, that for GCMC moves of dipoles is 2.2%, that for canonical moves of ions is 47.2%, and that for canonical moves of dipoles is 19.9%. The total CPU time required to obtain all data at $L^* = 12$, $T^* = 0.04762$, and $p^* = 0.60$ is 63 years for a single core of an Intel Xeon EM64T 3.0GHz. In total, I have used $\sim$150 CPU years to perform all simulations for this project.

4.2 Demixing with zero or weak dipole moment

I first want to investigate the simplest case. Namely, when "dipoles" do not have any interactions, how does the presence of hard spheres affects the phase behavior of the "ion–dipole" mixture? Figure 4.1(a) shows the density distributions of ions and hard spheres at $\mu^*_{\rm ion} = -1.3214$, $\mu^*_{\rm HS} = -0.1322$, $T^* = 0.04762$, and $L^* = 12$. The distribution for hard spheres has two distinct peaks corresponding to densities at $\rho^*_{\rm HS} \approx 0.02$ and $\rho^*_{\rm HS} \approx 0.05$, and the distribution for ions has two peaks at average densities $\rho^*_{\rm ion} \approx 0.01$ and $\rho^*_{\rm ion} \approx 0.22$. Two clearly observed peaks for both species indicates phase separation. The coexistence chemical potentials are calculated by using the equal-volume criterion [19, 20]. Figure 4.1(b) displays the two-dimensional density distribution for

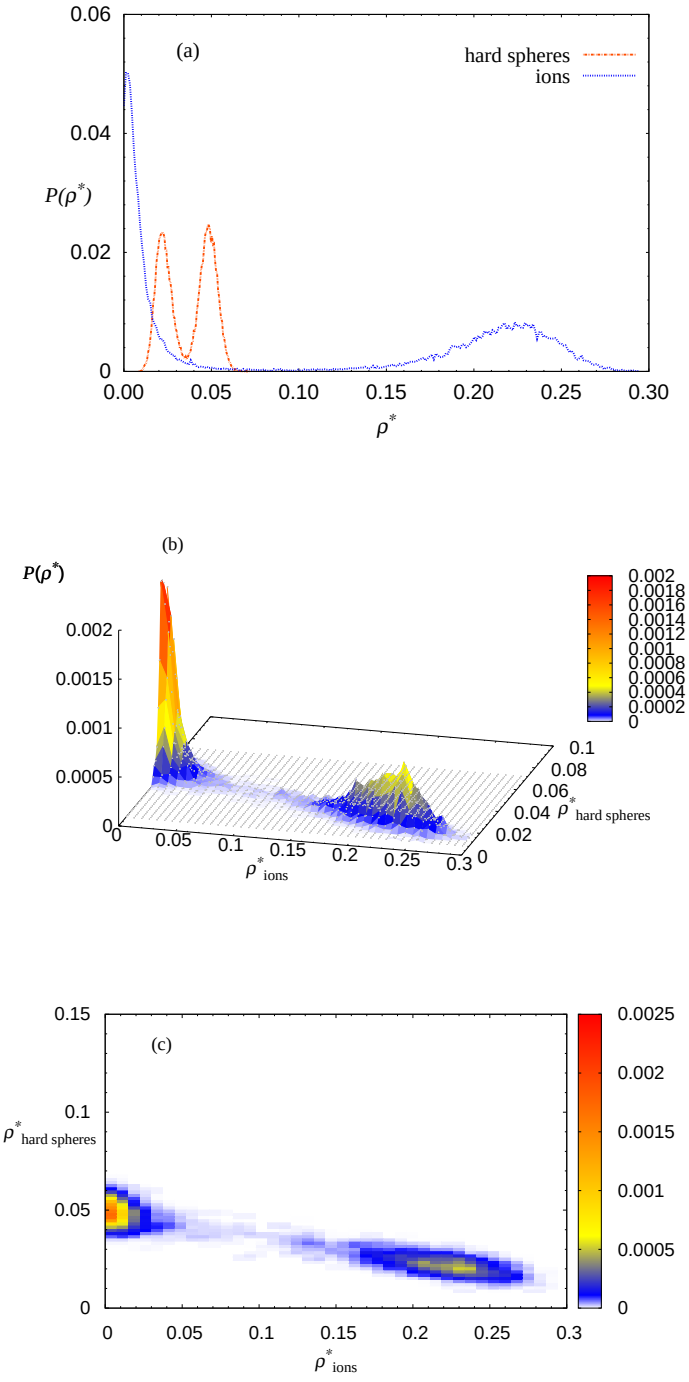

Figure 4.1: (a) Density distribution of an ion–hard sphere mixture at chemical potentials $\mu^*_{\text{ion}} = -1.3214$, $\mu^*_{\text{HS}} = -0.1322$, $T^* = 0.04762$, and $L^* = 12$. Two distinct peaks for each species indicate phase separation. (b) Two-dimensional density distribution of a mixture is plotted for same conditions as for (a). (c) Top view of the two-dimensional density distribution.

this mixture. When $\mu^*_{\rm ion}$ is scanned, the volume under each of the peaks in this figure varies as well. Phase coexistence corresponds to the situation where both volumes are equal. Figure 4.1(c) shows the top view of this distribution. Figures 4.1(b) and (c) show the ion-rich liquid phase and the ion-poor gas phase, which has been reported earlier by simulation [21] and theory [22].

This type of phase separation is a demixing process. In the dense liquid phase, the ionic interactions serve to lower the system energy at the cost of lower entropy. In this phase, hard spheres cannot help to lower the system energy. Therefore, when the ions form a dense phase, few hard spheres are present. In the gas phase, the total density is low and the system has a high entropy. Most of the hard spheres prefer to be in this gas phase to avoid mixing with ions, which would cause an increase in the energy of this system. For a very weak dipole moment $p^* = 0.1$, the same demixing phase behavior is still observed. Indeed, in this system, the dipolar temperature is $T^*_{\rm DHS} = 4.8$, i.e., the dipolar interaction is still very weak and the dipoles hardly interact with the ions.

4.3 Ionic phase separation with intermediate dipole moment

The previous section discussed demixing phase separation induced by adding hard spheres to ionic fluids. The next question is whether dipoles with an intermediate strength of the dipole moment can also cause phase separation. The dipole moment is increased to $p^* = 0.30$, corresponding to a dipolar temperature of $T^*_{\rm DHS} = 0.53$. As shown in Chapter 2, this dipole moment is still too weak to induce chain formation and isolated dipoles dominate the pure DHS fluid. However, dipoles start to interact with ions and other dipoles and this system clearly shows different behavior compared to the system with $p^* = 0$. Figure 4.2 shows the density distribution of each species at $T^* = 0.04762$ and $L^* = 12$. Distinct peaks in the ion density distribution ($\rho^*_{\rm ion} \approx 0.02$ and 0.16) are observed; however, the dipolar distribution has only a single low-density peak at $\rho^*_{\rm dipole} \approx 0.005$. At this intermediate dipolar interaction, dipoles start to connect with ions to lower the system energy, and demixing is prevented. Since pure ionic fluids can have a liquid–gas phase transition at this temperature, the ions still display phase separation when only a few dipoles are present as impurities.

In Fig. 4.3(a), I first fix the chemical potential for the dipoles and vary the chemical potential for the ions, thus changing the ionic composition. For $\mu^*_{\rm dipole} = -0.1510$, -0.1735, and -0.2070,

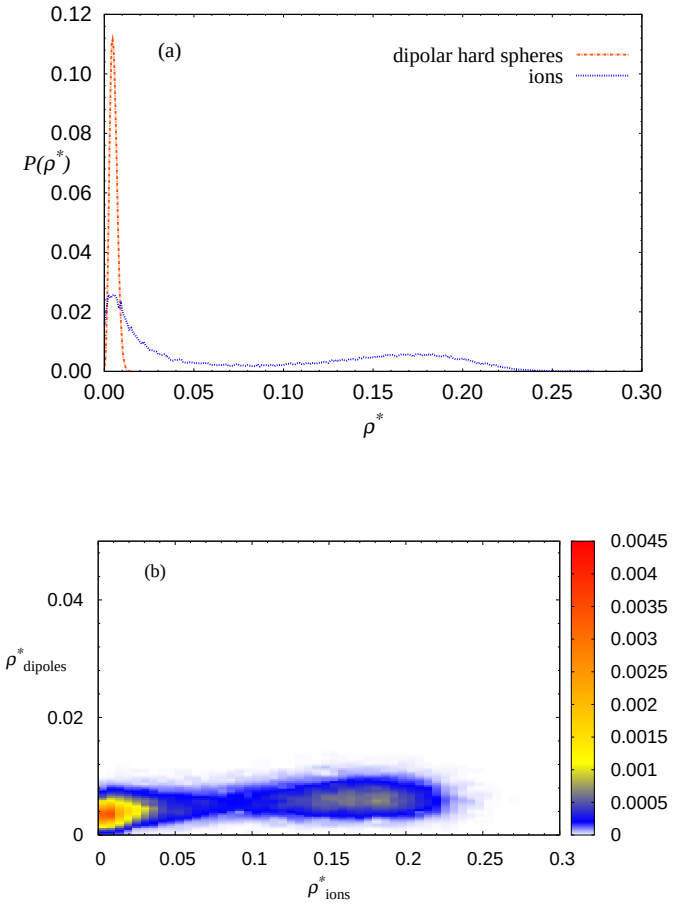

Figure 4.2: (a) Density distribution of an ion–dipole mixture at chemical potentials $\mu^*_{\text{ion}} = -1.3364$, $\mu^*_{\text{dipole}} = -0.2690$, $T^* = 0.04762$, $p^* = 0.30$ and $L^* = 12$. The ionic distribution has two peaks with average densities $\rho^*_{\text{ion}} \approx 0.02$ and $\rho^*_{\text{ion}} \approx 0.16$, whereas the dipoles display a single density peak at $\rho^*_{\text{dipole}} \approx 0.005$. (b) Top view of the two-dimensional density distribution of a mixture at the same conditions as for (a).

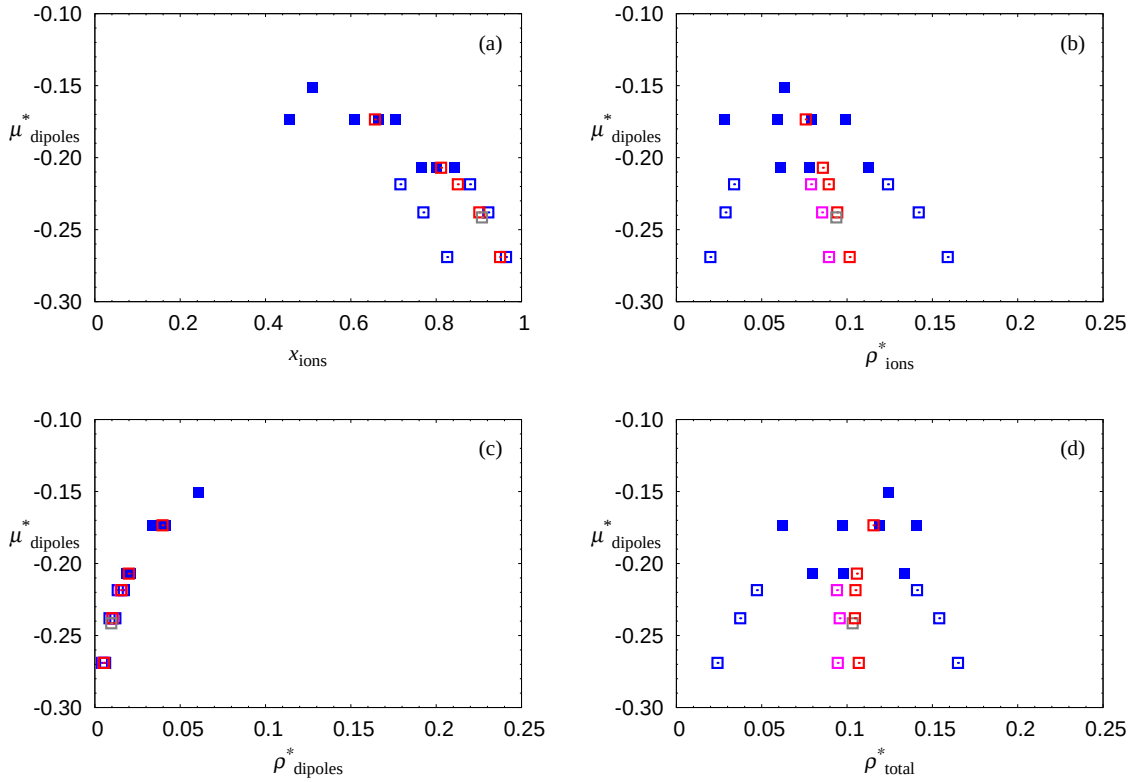

Figure 4.3: Phase diagrams of an ion–dipole mixture with $p^* = 0.30$ and $T^* = 0.04762$, for various planes of parameters. Filled squares indicate a single phase, open blue squares indicate coexisting phases (ρ^{*+}, ρ^{*-} are calculated directly from the observed distinct two peaks of the density distribution function), and open pink squares indicate the coexistence diameter $\overline{\rho^*}$. Red squares locate the maximum point of the Binder parameter Q at fixed dipolar chemical potentials and the gray square is the critical point. (a) Phase diagram of the ion–dipole mixture in the (μ^*_{dipole}, x_{ion}) plane. (b) Same figure in the (μ^*_{dipole}, ρ^*_{ion}) plane. (c) Same figure in the (μ^*_{dipole}, ρ^*_{dipole}) plane. (d) Same figure in the (μ^*_{dipole}, ρ^*_{total}) plane.

only homogeneous phases are found. These are indicated in Fig. 4.3 by the filled squares. When $\mu^*_{\rm dipole} \leq -0.2185$, I find phase coexistence between two ionic compositions, indicated by open blue squares. Changing the horizontal axis from the ionic composition to the ionic density, dipolar density or total density provides additional information. Figure 4.3(b) shows the ionic coexisting densities at dipolar chemical potentials $\mu^*_{\rm dipole} \leq -0.2185$. On the other hand, the dipolar density remains almost constant upon phase separation, as shown in Fig. 4.3(c).

Since I find phase separation in this mixture, the location of the critical point can be determined. To calculate the critical point, the Binder parameter (fourth-moment amplitude ratio) [7, 23, 24] is introduced,

$$Q_L = \frac{\langle m^2 \rangle^2}{\langle m^4 \rangle}, \tag{4.3}$$

where $m = \rho - \langle \rho \rangle$. It is known that when the system size goes to infinity, for the single phase region, the distribution of ρ becomes Gaussian, and $Q_L \to \frac{1}{3}$ [7, 23, 24]. In the two-phase region, $Q_L \to 1$ on the coexistence diameter $\overline{\rho} \equiv \frac{1}{2}(\rho^+ + \rho^-)$, where ρ^+ and ρ^- are the coexisting densities of liquid and gas at $T < T_c$. At criticality, Q_L approaches a nontrivial universal value Q_c which is $Q_c = 0.6236(2)$ for the Ising universality class [25]. The RPM shows $Q_c = 0.624(2)$, indicating that it belongs to this universality class [7]. In a single component Q_c is calculated as follows. At fixed temperature, Q_L is scanned by varying the chemical potential and the maximum of Q_L is recorded. This is repeated for various temperatures. At $T < T_c$, these maxima are found near the diameter $\overline{\rho}$. Q-loci on which Q_L is maximum at fixed T can be plotted for different system sizes, and the intersections $T_Q(L)$ between those curves are measured. In the thermodynamic limit, $T_Q(L) \to T_c$ and the corresponding critical value $Q_L(T_c)$ goes to Q_c [7].

Now, I want to apply this method to ion–dipole mixtures. $\mu^*_{\rm dipole}$ is fixed first and then $\mu^*_{\rm ion}$ is varied to find the maximum value of Q_L. In Figs. 4.3(b) and (d), open pink squares indicate the coexistence diameters and red squares are the maxima of the Binder parameter Q_L. For $\mu^*_{\rm dipole} < \mu^*_{\rm dipole,c}$, this locus of the maximum Q_L is located near the coexistence diameter $\overline{\rho^*}$. Figure 4.4 displays Q_L on the Q-loci at fixed $\mu^*_{\rm dipole}$ for $L^* = 8, 12, 15$. Since I only have Q-loci for three different system sizes, I simply measure the intersection of the curves for $L^* = 12$ and $L^* = 15$, and roughly estimate the critical value $\mu^*_{{\rm dipole},c} \approx \mu^*_{{\rm dipole},Q}(L^* = 15) \approx -0.245$, $\mu^*_{{\rm ion},c} \approx -1.337$, and $Q_c \approx 0.631$. Thus, this approach has not only provided the location of the critical point, but also shows that the critical behavior belongs to the Ising universality class. Interestingly, phase

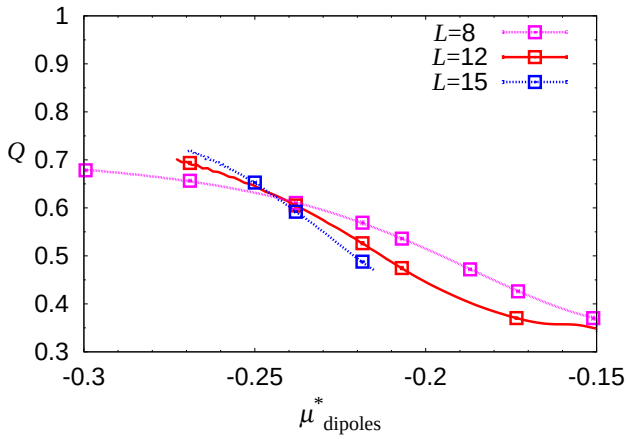

Figure 4.4: Maximum Binder parameter Q_L at fixed μ^*_{dipole} plotted as a function of dipolar chemical potential at $T^* = 0.04762$ for three different system sizes. The intersection point between two different system sizes yields the critical point $\mu^*_{\text{dipole},c}$, $\mu^*_{\text{ion},c}$, as well as Q_c.

separation still happens above the bulk critical point (a gray square) due to finite-size effects in Fig. 4.3. As the system size increases, I find that the maximum dipolar chemical potential that produces a liquid–gas phase transition decreases toward the measured critical point.

4.4 Phase separation with strong dipole moment

When the dipole moment is increased further to $p^* = 0.55$ (which corresponds to $T^*_{\text{DHS}} = 0.16$), dipoles tend to form chain structures and the nature of the phase separation changes. As shown in Fig. 4.5(a), the dipolar density distribution shows phase separation again, unlike for the mixture at $p^* = 0.30$, and both ions and dipoles have two peaks in the density distribution curve. More interestingly, Fig. 4.5(b) indicates that the gas phase has a low-density of both ions and dipoles, and the liquid phase has a high-density of both ions and dipoles, unlike the ion–hard sphere mixtures. In ion–dipole mixtures at dipole moment $p^* = 0.55$, the dipole–ion interaction energy is $-11.5k_BT$, much lower than the interaction at $p^* = 0.30$, where it is $-3.8k_BT$. Consequently, dipoles tend to strongly bind to ions, both phases have a similar ratio of ions to dipoles upon phase separation.

Figures 4.6(b) and (c) show that both ions and dipoles show a low-density and a high-density phase, whereas dipoles at $p^* = 0.30$ do not show phase separation in Fig. 4.3(c). In Fig. 4.6(a), the composition for both phases is almost the same. Although, this composition varies along the coexistence curve, the total densities in both the liquid and the gas phase remain roughly constant,

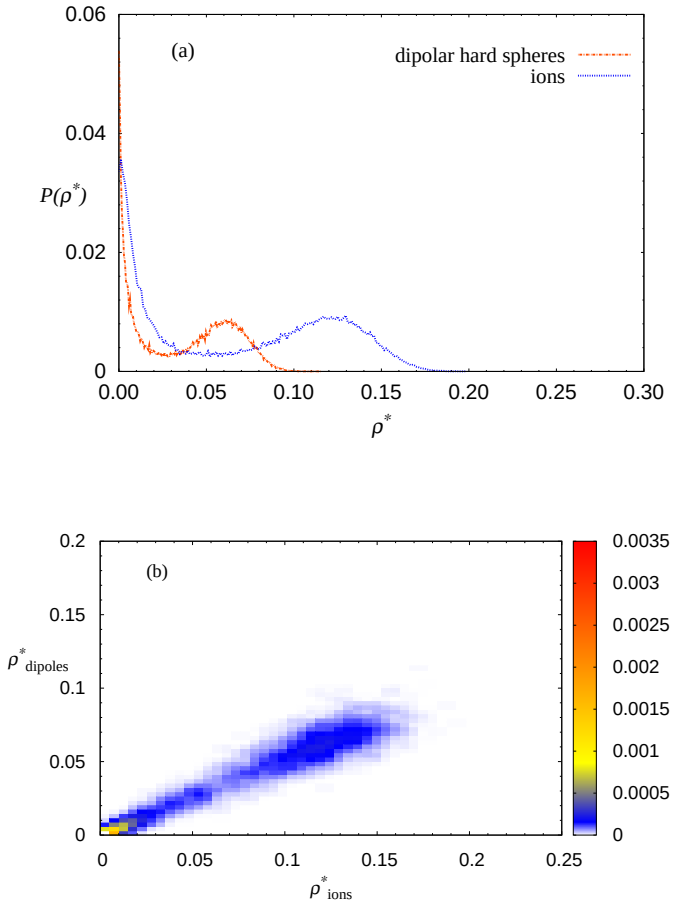

Figure 4.5: (a) Density distribution of an ion–dipole mixture at $\mu^*_{\text{ion}} = -1.3626$, $\mu^*_{\text{dipole}} = -0.3990$, $T^* = 0.04762$, $p^* = 0.55$ and $L^* = 12$. Two distinct peaks are observed for each species. Ions have two average densities at $\rho^*_{\text{ion}} \approx 0.017$ and 0.117, and dipoles have two average densities at $\rho^*_{\text{dipole}} \approx 0.009$ and 0.060. (b) Top view of the two-dimensional density distribution of a mixture at the same conditions as for (a).

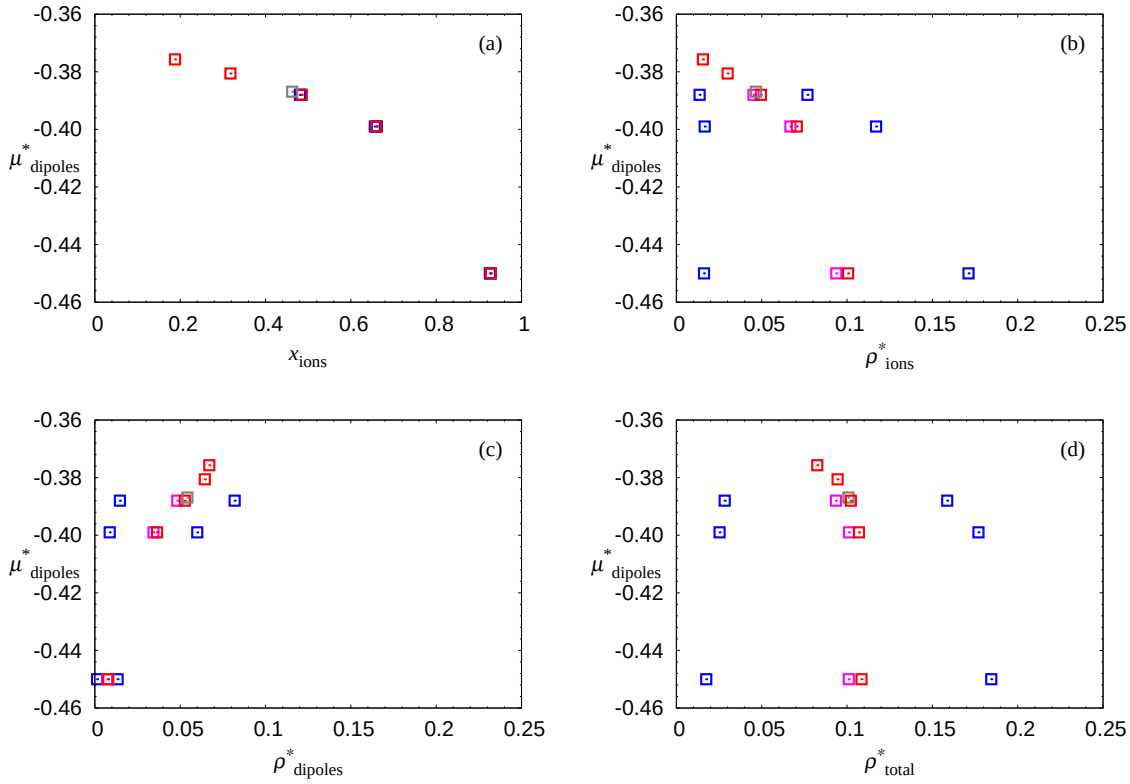

Figure 4.6: Phase diagrams of an ion–dipole mixture with $p^* = 0.55$ and $T^* = 0.04762$, for various planes of parameters. Open blue squares indicate coexisting phases, and open pink squares indicate the coexistence diameters. Red squares locate the maximum point of the Binder parameter Q_L at fixed μ^*_{dipole} and the gray square is the critical point. (a) The coexistence points of ion–dipole mixtures in the (μ^*_{dipole}, x_{ion}) plane. (b) Same figure in the (μ^*_{dipole}, ρ^*_{ion}) plane. (c) Same figure in the (μ^*_{dipole}, ρ^*_{dipole}) plane. (d) Same figure in the (μ^*_{dipole}, ρ^*_{total}) plane.

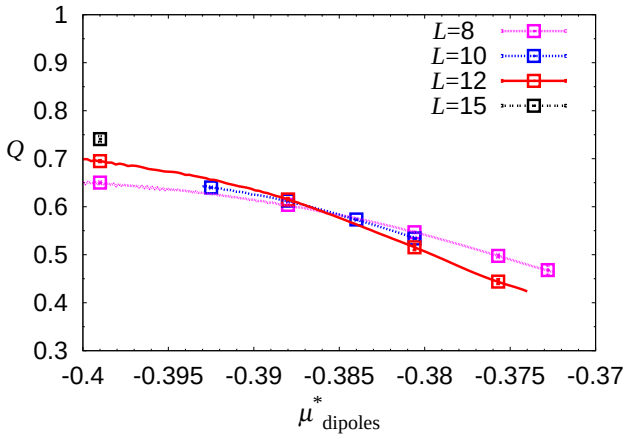

Figure 4.7: Plots of Q_L along the Q-loci, providing estimates for $\mu^*_{\text{dipole},c}$, $\mu^*_{\text{ion},c}$, and Q_c.

see Fig. 4.6(d). Finally, with decreasing ionic composition, phase separation disappears when the dipoles make up than 54% of the mixture. Figures 4.6(b), (c), and (d) show that the Q-loci obtained using the method described in the previous section are indeed located near the coexistence diameters. In Fig. 4.7, the critical point is estimated from the intersection of Q-loci using system sizes $L^* = 10$ and 12: this yields $\mu^*_{\mathrm{dipole},c} \approx -0.387$, $\mu^*_{\mathrm{ion},c} \approx -0.381$, and $Q_c \approx 0.602$. Lastly, at dipole moment $p^* = 0.6$ ($T^*_{\mathrm{DHS}} \approx 0.13$), dipoles bond even more strongly with ions and dipoles. As a result, the maximum dipole concentration that induces phase separation rises to 67%.

4.5 Structure

In the previous sections, I have found that the phase diagram of ion–dipole mixtures changes dramatically upon variation of the dipole moment. In this section, I will give quantitative descriptions of the structure of these ion–dipole mixtures. As in Chapter 2, the basic conformations of interest include rings, chains, and network clusters. Now, the ion and dipole composition of these clusters are also considered. In each case ($p^* = 0$, 0.3, 0.6), there is phase separation, and the gas phase is identified as the phase with low total density. The fractions of particles belonging to ion clusters, dipole clusters, ion–dipole clusters, ion monomers and dipole monomers in the gas phase at various dipole moments are shown in Fig. 4.8. When $p^* = 0$, the "dipoles" mostly remain as monomers because they do not have any interactions. At $p^* = 0.30$, the fraction of ion–dipole clusters in the gas phase becomes larger even though only few dipoles are present, because of the increased strength of the dipolar interactions. Since ion neutral pairs dominate the system at low temperature, a large portion of ion clusters is evident [6, 26]. When $p^* = 0.60$, the majority of structure is the ion–dipole clusters. This is consistent with the observation in the previous section that ions and dipoles are strongly bonded.

A resemblance of the structural properties of ion–dipole mixtures can be found in the dipole–hard sphere mixture [27, 28]. Phase separation occurs but long chains are not present in the dipole–hard sphere mixture. Indeed, at strong dipole moment, $p^* = 0.60$, if I compare the pure DHS system with $\rho^*_{\mathrm{dipole}} = 0.12$ and the mixture with $\rho^*_{\mathrm{ion}} = 0.08$ and $\rho^*_{\mathrm{dipole}} = 0.04$, the pure DHS system has an average chain length 11.3 while the mixture has an average chain length 3.2 (chains include ions and dipoles). This confirms that when mixtures undergo phase separation, long chains

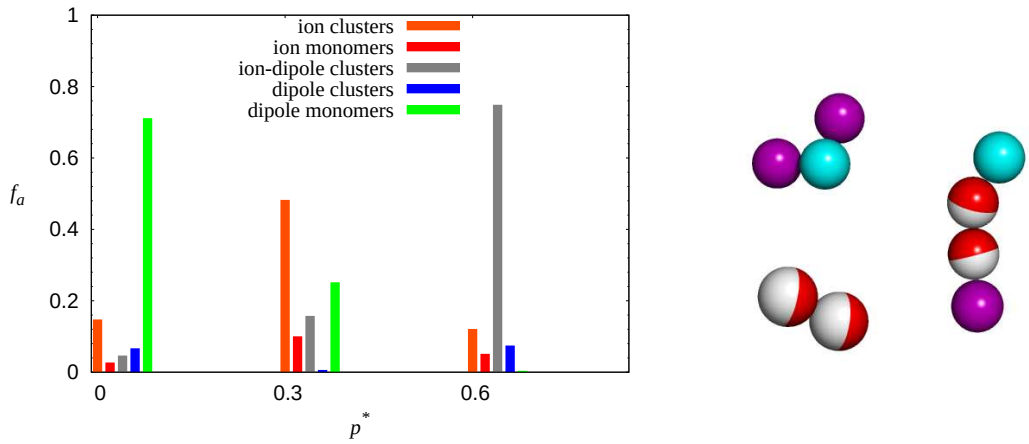

Figure 4.8: Structural change in the gas phase for different dipolar strengths ($L^* = 8$). Purple spheres are positive ions, cyan spheres are negative ions, and half red and half white spheres are dipoles. Typical structures of ion clusters, dipole clusters, and ion–dipole clusters are illustrated.

are not present, unlike the system of the pure DHS. It seems that strongly bonded long chains in the pure DHS system have some role preventing phase separation, in agreement with earlier theoretical suggestions [29–31].

4.6 Summary and conclusions

In this simulation study, temperature controls the strength of ionic interactions, and it is kept fixed at $T^* = 0.04762$, where phase separation happens in pure ionic fluids. I investigate the phase behavior of ion–dipole mixtures with various dipole moments. Qualitatively different phase diagrams are found by varying the ratio of the dipolar to the ionic interaction. When the dipole moment is very weak, demixing is observed. At intermediate dipole strength, phase separation disappears in a large region of the (μ^*_{dipole}, x_{ion}) plane, and there are few dipoles present when phase separation happens. When the dipole moment is strong enough to bond ion–dipole pairs, a liquid–gas phase transition returns. In this mixture, the relative ion–dipole fraction is roughly constant for both coexisting phases, and the ionic composition can be less than 50%. This type of phase separation is neither demixing nor ionic phase separation, but the same ratio of the number of ions to the number of dipoles undergoes phase separation. This behavior has not been reported before.

4.7 References

[1] J. J. van Laar, “On the different forms and transformations of the boundary-curves in the case of partial miscibility of two liquids,” Proc. Kon. Akad. **7**, 636–645 (1905).

[2] R. L. Scott and P. H. Van Konynenburg, “Van der Waals and related models for Hydrocarbon mixtures,” Discuss. Faraday Soc. **49**, 87–97 (1970).

[3] P. H. Van Konynenburg and R. L. Scott, “Critical lines and phase equilibria in binary Van der Waals mixtures,” Phil. Trans. Roy. Soc. London **298**, 495–540 (1980).

[4] J. S. Rowlinson and F. L. Swinton, *Liquids and liquid mixtures*, 3rd ed. (Butterworths, London, 1982).

[5] R. L. Scott, “Models for phase equilibria in fluid mixtures,” Acc. Chem. Res. **20**, 97–107 (1987).

[6] G. Orkoulas and A. Z. Panagiotopoulos, “Free energy and phase equilibria for the restricted primitive model of ionic fluids from Monte Carlo simulations,” J. Chem. Phys. **101**, 1452–1459 (1994).

[7] E. Luijten, M. E. Fisher and A. Z. Panagiotopoulos, “Universality class of criticality in the restricted primitive model electrolyte,” Phys. Rev. Lett. **88**, 185701 (2002).

[8] J. S. Høye, E. Lomba and G. Stell, “Mean spherical approximation for a simple model of electrolytes. II. Correlation functions and thermodynamics: Numerical results,” J. Chem. Phys. **89**, 7462–7470 (1988).

[9] A. H. Harvey, “Phase equilibria and critical lines in model water/salt mixtures,” J. Chem. Phys. **95**, 479–484 (1991).

[10] R. Thiéry, S. N. Lvov and J. Dubessy, “A global phase diagram for the ion–dipole model in the mean spherical approximation,” J. Chem. Phys. **109**, 214–222 (1998).

[11] K.-Y. Chan, K. E. Gubbins, D. Henderson and L. Blum, “Monte Carlo and simple theoretical calculations for ion–dipole mixtures,” Mol. Phys. **66**, 299–316 (1989).

[12] J. M. Caillol, D. Levesque and J. J. Weis, “Monte Carlo simulation of an ion–dipole mixture,” Mol. Phys. **69**, 199–208 (1990).

[13] J. Eggebrecht and P. Ozler, “Multipolar electrolyte solution models. I. Computer simulation of the charged and dipolar hard sphere mixture,” J. Chem. Phys. **93**, 2004–2015 (1990).

[14] W. Y. Lo, K.-Y. Chan and D. Henderson, “Improved Monte Carlo simulations of the structure of ion–dipole mixtures,” Mol. Phys. **80**, 1021–1029 (1993).

[15] J. C. Shelley and G. N. Patey, “Phase behavior of ionic solutions: Comparison of the primitive and explicit solvent models,” J. Chem. Phys. **110**, 1633–1637 (1999).

[16] D. Frenkel and B. Smit, *Understanding Molecular Simulation*, 2nd ed. (Academic, San Diego, 2002).

[17] S. W. de Leeuw, J. W. Perram and E. R. Smith, “Simulation of electrostatic systems in periodic boundary conditions. I. Lattice sums and dielectric constants,” Proc. R. Soc. London, Ser. A **373**, 27–56 (1980).

[18] B. Widom, “Some topics in the theory of fluids,” J. Chem. Phys. **39**, 2808–2812 (1963).

[19] C. Borgs and S. Kappler, “Equal weight versus equal height: a numerical study of an asymmetric first-order transition,” Phys. Lett. A **171**, 37–42 (1992).

[20] V. K. Shen and J. R. Errington, “Determination of fluid-phase behavior using transition-matrix Monte Carlo binar Lennard-Jones mixtures,” J. Chem. Phys. **122**, 064508 (2005).

[21] T. Kristóf, D. Boda, I. Szalai and D. Henderson, “A Gibbs ensemble Monte Carlo study of phase coexistence in the solvent primitive model,” J. Chem. Phys. **113**, 7488–7491 (2000).

[22] Y. Zhou and G. Stell, “Criticality of charged systems. II. The binary mixture of hard spheres and ions,” J. Chem. Phys. **102**, 5796–5802 (1995).

[23] K. Binder, “Finite size scaling analysis of Ising-model block distribution functions,” Z. Phys. B **43**, 119–140 (1981).

[24] Y. C. Kim, M. E. Fisher and E. Luijten, “Precise simulation of near-critical fluid coexistence,” Phys. Rev. Lett. **91**, 065701 (2003).

[25] H. W. J. Blőte, E. Luijten and J. R. Heringa, “Ising universality in three dimensions: a Monte Carlo study,” J. Phys. A **28**, 6289–6313 (1995).

[26] M. J. Gillan, “Liquid–vapour equilibrium in the restricted primitive model for ionic liquids,” Mol. Phys. **49**, 421–442 (1983).

[27] M. J. Blair and G. N. Patey, “Gas–liquid coexistence and demixing in systems with highly directional pair potentials.,” Phys. Rev. E **57**, 5682–5686 (1998).

[28] N. G. Almarza, E. Lomba, C. Martín and A. Gallardo, “Demixing in binary mixtures of apolar and dipolar hard spheres,” J. Chem. Phys. **129**, 234504 (2008).

[29] R. P. Sear, “Low-density fluid phase of dipolar hard spheres,” Phys. Rev. Lett. **76**, 2310–2313 (1996).

[30] R. van Roij, “Theory of chain association versus liquid condensation,” Phys. Rev. Lett. **76**, 3348–3351 (1996).

[31] Y. Levin, “What happened to the gas-liquid transition in the system of dipolar hard spheres?,” Phys. Rev. Lett. **83**, 1159–1162 (1999).

CHAPTER 5

DIFFUSION OF ADSORBED POLYMERS

Understanding the lateral diffusion of adsorbed polymers at a solid–liquid interface is important for a wide range of applications—from coatings and adhesives to tribology—as well as from a fundamental point of view. Although this topic has received considerable attention over the past decade, both experimentally [1–6] and from computer simulations [7–12], most work has focused on single-chain behavior under dilute conditions. The *collective* diffusive behavior of adsorbed polymers has received comparatively little attention. Zhao and Granick [13] studied the diffusion of polyethylene glycol (PEG) on silica surfaces that were rendered hydrophobic, as a function of surface coverage. Remarkably, they observed that the lateral diffusion coefficient *increases* monotonically with surface coverage, followed by a sudden drop once a threshold coverage has been reached. This threshold is tentatively associated with the onset of monolayer coverage, whereas the initial increase of the diffusivity is ascribed to conformational changes of the adsorbed polymers. In view of the difficulty of testing these interpretations experimentally, and given the scarcity of results for collective diffusion of adsorbed polymers in even the simplest computational models, I investigate these properties by means of molecular dynamics (MD) simulations. I do not aim to incorporate all aspects of the experimental system, but rather wish to elucidate the behavior of a system that can serve as a reference in the interpretation of these and future experiments.

Prior simulation studies for dilute chains have shown that various parameters, including surface corrugation [12], the presence of obstacles [8, 11], and the inclusion of explicit solvent [10], can affect diffusive properties. It is plausible that these parameters will also be important at higher surface coverage. Nevertheless, since extant work at such coverages almost exclusively focuses on static properties for the simplest models [14, 15], I feel justified to confine myself here to the dynamic behavior of polymers adsorbed on a smooth, obstacle-free surface in the presence of an implicit solvent.

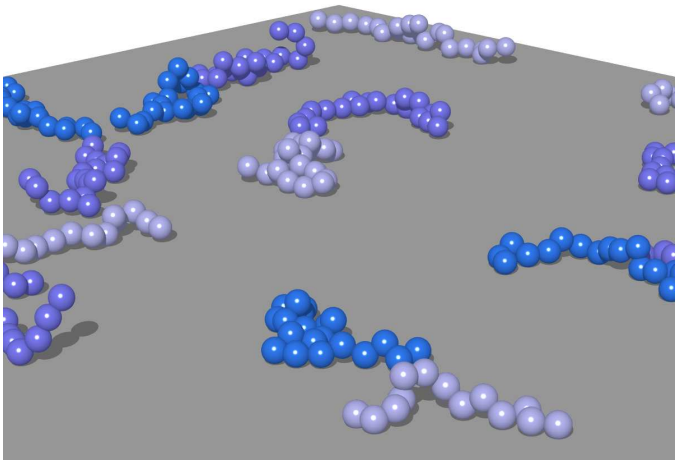

Figure 5.1: Snapshot of adsorbed polymers with $N = 20$, $\varepsilon_w = 3\varepsilon_a$, $\phi_m = 0.09$. Each sphere represents a Kuhn segment and each polymer is adsorbed onto a flat surface.

5.1 Simulation methodology

I study a bead–spring model of monodisperse linear chains, which is shown in Fig. 5.1. The monomers represent Kuhn segments and interact via a shifted-truncated Lennard-Jones (LJ) potential,

$$U_{\mathrm{LJ}}(r) = \begin{cases} 4\varepsilon\left[\left(\frac{\sigma}{r}\right)^{12} - \left(\frac{\sigma}{r}\right)^{6}\right] + \varepsilon & \text{if } r \le r_c \\ 0 & \text{if } r > r_c \end{cases} . \tag{5.1}$$

Here, $r = |\mathbf{r}_i - \mathbf{r}_j|$ is the center-to-center distance between monomers i and j. I use the monomer diameter σ as the unit of length and ε as the unit of energy. The cutoff distance is set to $r_c = 2^{1/6}\sigma$, i.e., at the minimum of the LJ potential. Therefore, the system is always in the good-solvent regime. Adjacent monomers on the same chain are bonded via a finite extensible nonlinear elastic (FENE) potential [16],

$$U_{\mathrm{FENE}}(r) = -\frac{1}{2}kR_0^2 \ln\left[1 - \left(\frac{r}{R_0}\right)^2\right] . \tag{5.2}$$

I select the parameters $R_0 = 1.5\sigma$, $k = 30\varepsilon/\sigma^2$, permitting a reasonably large time step [16]. The total pair interaction between connected monomers is the sum of the shifted-truncated LJ potential and the FENE potential, with a minimum at $r \approx 0.93\sigma$. The simulation cell has dimensions $L \times L \times D$ and is periodically replicated in the x and y directions. Two surfaces, oriented parallel to the x–y plane, are placed at the top and the bottom of the cell, respectively. The height of the simulation cell is kept fixed at $D = 50\sigma$ and the linear system size ranges from $L = 40\sigma$ to $L = 400\sigma$.

To avoid finite-size effects, L is always chosen to exceed four times the end-to-end distance R of an individual chain. The surfaces are treated as a continuum, so that the interactions between the monomers and the surface can be represented through a 9–3 Lennard-Jones potential [17],

$$U_w(z) = \varepsilon_w \left[\left(\frac{\sigma_{wm}}{z} \right)^9 - q \left(\frac{\sigma_{wm}}{z} \right)^3 \right], \tag{5.3}$$

where z is the vertical distance from the surface and $\sigma_{wm} = 0.6494\sigma$. The top surface is purely repulsive, $q = 0$, whereas the bottom surface represents the adsorbing interface, with $q = 7.5$. The surface interaction takes its minimum $U_w \approx -7.91\varepsilon_w$ at $z_{\min} = (3/q)^{1/6}\sigma_{wm} \approx 0.56\sigma$. I investigate both weak and strong adsorption regimes, choosing $\varepsilon_w = 2\varepsilon_a$, $3\varepsilon_a$, $4\varepsilon_a$, and $6\varepsilon_a$, where ε_a indicates the adsorption threshold energy.

To estimate the adsorption threshold energy, I first perform configurational-bias Monte Carlo (CBMC) simulations [18] of a single chain with one end grafted to the attractive surface, and determine the radius of gyration parallel and perpendicular to the surface,

$$R_{g\parallel} \equiv \langle 0.5(R_{gx}^2 + R_{gy}^2) \rangle^{1/2}, \tag{5.4}$$

$$R_{g\perp} \equiv \langle R_{gz}^2 \rangle^{1/2}. \tag{5.5}$$

Here R_{gx}, R_{gy} and R_{gz} are the x,y and z components of the radius of gyration. Near the adsorption threshold, the ratio $R_{g\perp}/R_{g\parallel}$ is predicted to scale as [17]

$$\frac{R_{g\perp}}{R_{g\parallel}} \propto \begin{cases} \text{const} & x \to +\infty \\ \text{const}' & x = 0 \\ |x|^{-\nu_{d=2}/\varphi} & x \to -\infty \end{cases}, \tag{5.6}$$

where $x = \tau N^{\varphi}$ ($\tau = 1 - \varepsilon_w/\varepsilon_a$), $\nu_{d=2} = \frac{3}{4}$ is the scaling exponent in two dimensions, and $\varphi = \frac{1}{2}$ is the crossover exponent [17, 19]. Thus, when the ratio $R_{g\perp}/R_{g\parallel}$ is plotted as a function of ε_w, the curves for different chain lengths are predicted to converge, in the limit of large chain length, to zero for strong adsorption energies and to a finite constant for weak adsorption energies. At $\varepsilon_w = \varepsilon_a$ the curves intersect. This is confirmed in Fig.5.2. I find slightly different intersection points for different pairs of chain lengths and adopt the arithmetic mean, $\varepsilon_a = 0.002475 \pm 0.000006$, as my

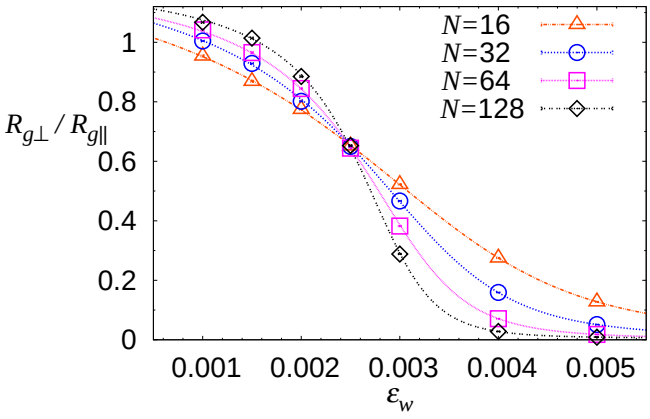

Figure 5.2: Ratio $R_{g\perp}/R_{g\parallel}$ *versus* adsorption energy ε_w for four different chain lengths. Symbols are calculated from simulations and curves are calculated by histogram reweighting [20]. The intersection between the four curves provides the threshold adsorption energy $\varepsilon_a = 0.002475 \pm 0.000006$.

estimate for the adsorption threshold.

In my simulations, the strongest adsorption energy is $\varepsilon_w = 6\varepsilon_a$, corresponding to a "sticking energy" of approximately $-0.12k_BT$ per monomer. This is not strong enough to reach monolayer coverage (I achieve a maximum surface coverage of approximately 70%), in line with the fact that this value is significantly below the estimated sticking energy of PEG on silica surfaces, $-0.5k_BT$ per monomer [4]. I deem a monomer adsorbed if it lies within a distance $z = 1.3\sigma$ from the bottom interface. The surface monomer density is then defined as $\phi_m = N_m/L^2$, where N_m is the total number of adsorbed monomers. For all four choices of the adsorption strength ε_w I investigate a large number of surface coverages $0.01 \leq \phi_m \leq 0.7$, for five different chain lengths, $N = 20$, 40, 60, 80, and 160, comparable to the experimental degree of polymerization of 244 [13] (the persistence length of PEG corresponds to only a few monomers). The systems contain between 10 and 72 polymer chains. Table 5.1 summarizes the linear system sizes L and number of chains N_c used in the different simulations, along with the surface monomer coverage that would result if all monomers would adsorb, $\phi_{\max} \equiv NN_c/L^2$.

Since the relaxation time increases rapidly with chain length and surface coverage, I employ CBMC simulations to efficiently create initial configurations for all these cases. Subsequently, I use the resulting configurations, in which now all constraints are lifted, to perform MD simulations using the LAMMPS package [21]. Prior to sampling any properties, the systems are further equilibrated using MD. Typical configurations are depicted in Fig. 5.3. The time step is $\Delta\tau = 0.003\tau$,

	$N = 20$		$N = 40$		$N = 60$		$N = 80$		$N = 160$	
$\phi_{\max}$	N_c	L	N_c	L	N_c	L	N_c	L	N_c	L
0.01	20	200	40	400	24	380	20	400	10	400
0.1	18	60	25	100	24	120	18	120	18	170
0.2	36	60	32	80	48	120	36	120	–	–
0.4	72	60	36	60	54	90	50	100	25	100
0.6	48	40	54	60	49	70	48	80	39	102
0.8	64	40	50	50	48	60	36	60	–	–

Table 5.1: Simulation parameters for different chain lengths and surface densities. The system size L is decreased for higher densities to avoid simulations with too large a number of chains. However, to prevent self interactions between a chain and its periodic images, L is always chosen to exceed four times the end-to-end distance.

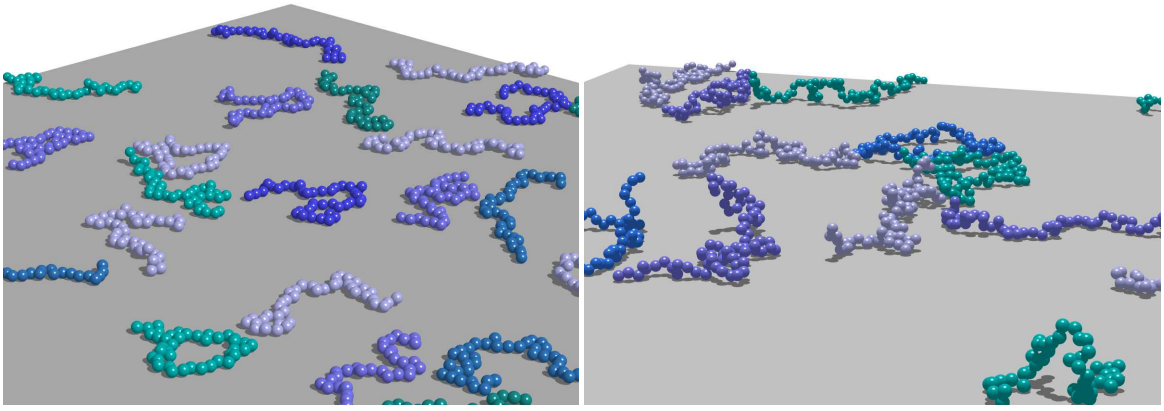

Figure 5.3: Typical configurations at low surface coverage. (a) Snapshot for chain length $N = 40$, adsorption energy $\varepsilon_w = 6\varepsilon_a$, and surface density $\phi_m = 0.1$. As illustrated, "flat" conformations are observed at high adsorption energy and low surface coverage. (b) Typical configuration for chain length $N = 80$, adsorption energy $\varepsilon_w = 2\varepsilon_a$, and surface density $\phi_m = 0.07$. At this lower adsorption strength, "loop–train–tail" conformations are observed, causing ϕ_m to be smaller than $\phi_{\max} = 0.1$.

where $\tau = (\sigma^2 m/\varepsilon)^{1/2}$, and m is the monomer mass. The sampling interval is chosen to be roughly the characteristic time for the center of mass of a polymer chain to move over its end-to-end distance. This sampling interval varies from $1.5 \times 10^4 \Delta\tau$ to $2.5 \times 10^5 \Delta\tau$ and depends on chain length, adsorption energy, and surface density. After the system has been equilibrated, 1250–25000 samples are recorded. The diffusion coefficient is calculated from the lateral mean square displacement of the polymers,

$$g_{\mathrm{cm}\parallel}(t) = \frac{1}{N_c} \sum_{i=1}^{N_c} \left\langle \left[\mathbf{R}_{i,\mathrm{cm}\parallel}(t+t_0) - \mathbf{R}_{i,\mathrm{cm}\parallel}(t_0) \right]^2 \right\rangle . \tag{5.7}$$

Here, $\mathbf{R}_{i,\mathrm{cm}\parallel}(t)$ denotes the center-of-mass position of chain i at time t and $\langle\cdot\rangle$ means the ensemble average over all time origins t_0. Assuming that the polymers undergo Brownian motion, the diffusion coefficient D can be measured from the mean square displacement via $4Dt = g_{\mathrm{cm}\parallel}(t)$.

The temperature is fixed to $k_B T/\varepsilon = 1$ using a Langevin thermostat. The equation of motion for monomer j is [22]

$$m\frac{d^2\mathbf{r}_j}{dt^2} = \mathbf{F}_j(\mathbf{r}_j) - \gamma m \frac{d\mathbf{r}_j}{dt} + \mathbf{R}_j(t) . \tag{5.8}$$

The first term, $\mathbf{F}_j(\mathbf{r}_j)$, is the force on monomer j induced by the pairwise interactions between monomers. The remaining contributions to the force result from the implicit solvent–monomer interactions. Solvent molecules drag the monomer with a friction coefficient ζ, i.e., $\mathbf{F}_{\mathrm{friction}} = -\zeta \mathbf{v}_j$, where $\mathbf{v}_j$ is the monomer velocity. The friction coefficient is related to the collision frequency $\gamma = \zeta/m$ and I choose $\gamma = 0.1\tau^{-1}$ [16]. In addition, the random force $\mathbf{R}_j(t)$ represents the collisions with solvent molecules, resulting from thermal fluctuations.

5.2 Diffusion coefficient

Experimentally, various power-law dependences on chain length have been found for the diffusion coefficient in the dilute regime. For polymers diffusing on lipid bilayers, the diffusion coefficient scales as $D \sim N^{-1}$ [1,5]. However, on a solid surface D was found to scale as $N^{-1.5}$ [3]. To clarify the situation for my model, I first simulate the surface diffusion of chains in the dilute regime, $\phi_m = 0.01$, for N between 20 and 320. As shown in Fig. 5.4, I find strong evidence for an inverse linear proportionality, $D \sim N^{-1.018\pm0.009}$.

Figure 5.5(a) shows the lateral diffusion coefficient as a function of surface monomer density

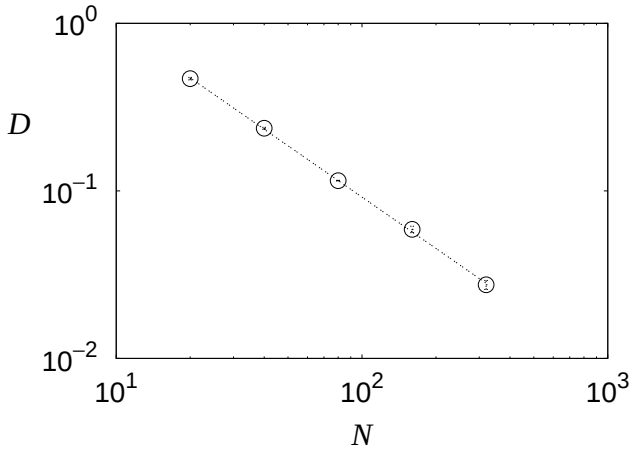

Figure 5.4: Lateral diffusion coefficient D in the dilute regime ($\phi_m = 0.01$, $\varepsilon_w = 6\varepsilon_a$) as a function of chain length N ($20 \leq N \leq 320$), on a logarithmic scale. The diffusion coefficient scales as $D \sim N^{-1.018\pm0.009}$.

for $N = 40$ and all four adsorption strengths. The diffusion coefficient decreases *monotonically* with increasing surface monomer coverage. Moreover, the data for different adsorption energies coincide. However, since I omit data for conditions where chain desorption occurs (indicated by the arrows in Fig. 5.5(a)), the data extend to larger surface coverage for higher adsorption strengths. The diffusion of adsorbed chains is typically assumed to be related to their conformation. However, coinciding diffusion coefficients at identical surface coverage do *not* imply identical chain configurations. This is illustrated in Fig. 5.5(b), which displays the lateral diffusion coefficient *versus* the fraction of adsorbed monomers. Since both panels in Fig. 5.5 employ the same vertical scale, the relation between chain conformation and surface monomer coverage can be deduced. At low adsorption strength, $\varepsilon_w = 2\varepsilon_a$, already in the dilute regime ($D \approx 0.25$) chains are only partially adsorbed, adopting so-called "loop–train–tail" conformations where the chain ends are typically not adsorbed and the other monomers alternate between short sequences of adsorbed units ("trains") and desorbed units ("loops") [23]. For higher adsorption strengths, more than 90% (increasing with increasing ε_w) of the monomers is adsorbed in the dilute regime, corresponding to "flat" configurations. Nevertheless, these chains display the same center-of-mass diffusion coefficient if the total number of adsorbed monomers is the same as for systems with lower adsorption strengths. In addition, Fig. 5.5(b) shows that initially the *fraction* of adsorbed monomers remains almost constant with increasing coverage, even though the diffusion rate decreases. Thus, I infer from these results that the mobility of adsorbed polymers is controlled by the total number of adsorbed monomers. In-

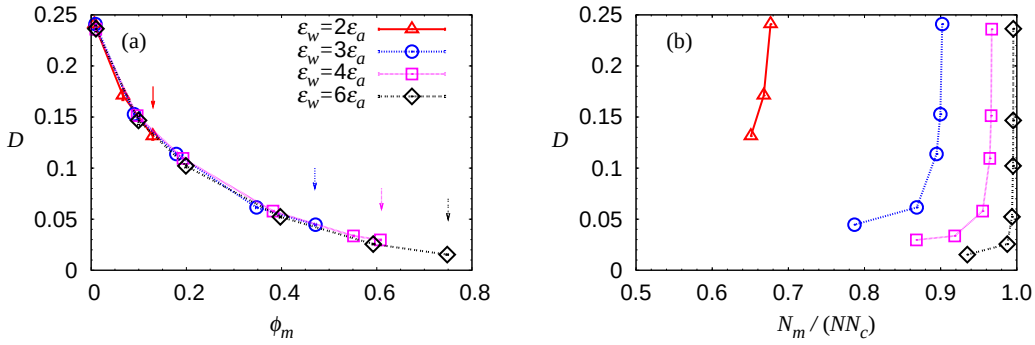

Figure 5.5: (a) Lateral diffusion coefficient $D(\sigma^2/\tau)$ as a function of surface monomer coverage for chain length $N = 40$ and various adsorption energies ε_w. Error bars are smaller than the symbol size. (b) Lateral diffusion coefficient versus the fraction of adsorbed monomers.

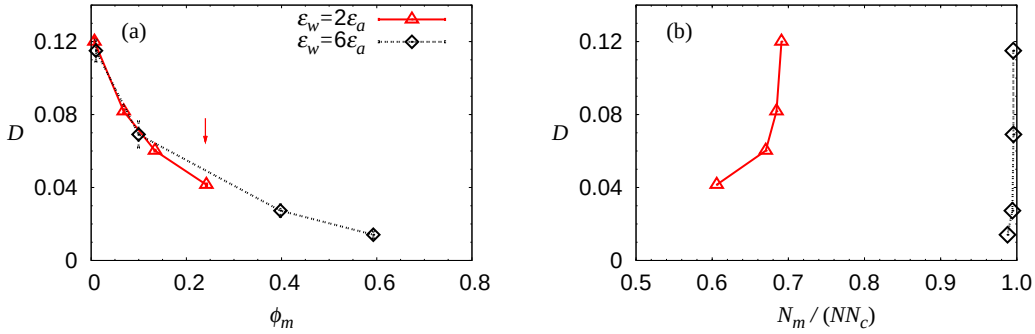

Figure 5.6: (a) Lateral diffusion coefficient D as a function of surface monomer coverage for chain length $N = 80$ and various adsorption energies ε_w. (b) Lateral diffusion coefficient versus the fraction of adsorbed monomers.

deed, ultimately, just prior to the onset of desorption, the fraction of adsorbed monomers decreases and chains adopt "loop–train–tail" conformations even at high adsorption strengths. However, this conformational change does not lead to an increased mobility. I also investigate the diffusion behavior for different chain lengths. As illustrated in Fig. 5.6 for $N = 80$, longer chains have a higher maximum surface coverage at the same adsorption energy ($\varepsilon_w = 2\varepsilon_a$). For $\varepsilon_w = 6\varepsilon_a$, I do not simulate the system at surface densities higher than $\phi_{\max} = 0.6$ because of the computational cost. The overall behavior of diffusion and conformational change is similar to the results for chain length $N = 40$.

I repeat these simulations for chain lengths $N = 40$, 60, 80, and 160. Figure 5.7 reveals several remarkable properties of the diffusion coefficient. First, the behavior observed in Fig. 5.5(a) for $N = 40$ is accurately described by an exponential function of surface coverage. Secondly, this behavior

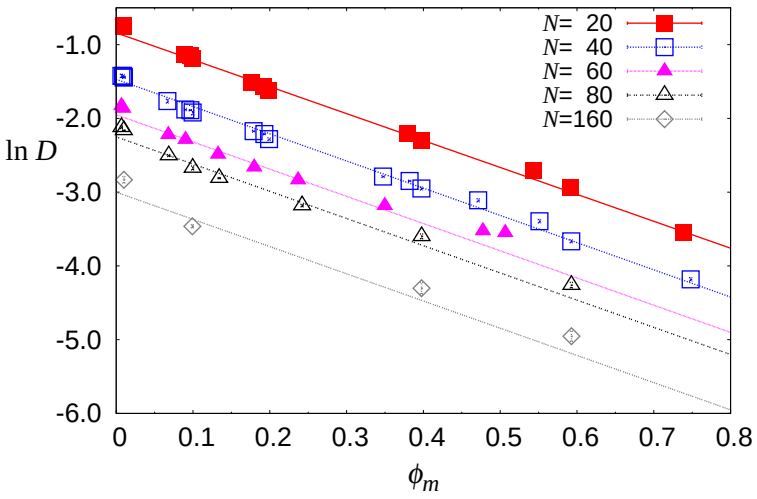

Figure 5.7: Logarithmic diffusion coefficient as a function of surface monomer density for different chain lengths.

is recovered for other chain lengths (with a statistical accuracy that diminishes with increasing chain length, owing to computational costs), with an exponential decay that is *independent* of N. Thus, as a corollary, the $1/N$ dependence observed in the dilute regime *persists* with increasing surface coverage. For $N = 20$, I find $D \propto \exp(-b\phi_m)$ with $b = 3.65 \pm 0.08$, and the straight lines in Fig. 5.7 represent $D \propto N^{-1}\exp(-b\phi_m)$. My results can be viewed as a generalization of earlier findings (obtained via MC simulations) for polymers confined to a narrow slit. Ref. [24] found an exponential increase of the relaxation time τ with increasing polymer density, which is consistent with my findings, since $D \sim R^2/\tau$. For branched polymers, Ref. [25] also observed an exponential decrease of the diffusion coefficient. Most importantly, none of these findings indicates an increase of the diffusion coefficient with increasing concentration.

5.3 Summary and conclusions

My simulations provide compelling evidence that adsorbed polymers diffuse progressively slower with increasing surface coverage, *irrespective* of conformational changes that occur as the environment becomes more crowded. This is at variance with the arguments put forward in Ref. [13], namely that a decreased number of adsorption sites per chain leads to an enhanced mobility. Evidently, this still leaves the original experimental findings to be explained. I note that in the pertinent regime the experimental uncertainties are rather large, making it difficult to unequivocally claim an

increasing trend (although there is no evidence of a systematic decrease either). The second anomalous feature observed in the experiment, namely an abrupt decrease of the diffusion coefficient near monolayer coverage [13], is out of reach for the adsorption strengths employed here, which limit the surface coverage to approximately 70%. Despite this limitation, my findings can be viewed as a reference for the collective diffusion behavior of model polymers at sub-monolayer coverage.

Finally, I comment briefly on recent simulation studies [26, 27] that appear to reproduce the experimental findings of Ref. [13]. These simulations do not only employ oligomers that are far shorter than the chains in the experiment, but also focus on the poor-solvent regime where the chains for a single globular phase [27]. This is in stark contrast with the experiments, for which it is explicitly reported that no aggregation is observed.

5.4 References

[1] B. Maier and J. O. Rädler, "Conformation and self-diffusion of single DNA molecules confined to two dimensions," Phys. Rev. Lett. **82**, 1911–1914 (1999).

[2] B. Maier and J. O. Rädler, "DNA on fluid membranes: A model polymer in two dimensions," Macromolecules **33**, 7185–7194 (2000).

[3] S. A. Sukhishvili, Y. Chen, J. D. Müller, E. Gratton, K. S. Schweizer and S. Granick, "Diffusion of a polymer 'pancake'," Nature **406**, 146 (2000).

[4] S. A. Sukhishvili, Y. Chen, J. D. Müller, E. Gratton, K. S. Schweizer and S. Granick, "Surface diffusion of poly(ethylene glycol)," Macromolecules **35**, 1776–1784 (2002).

[5] L. Zhang and S. Granick, "Slaved diffusion in phospholipid bilayers," Proc. Natl. Acad. Sci. U.S.A. **102**, 9118–9121 (2005).

[6] D. Nykypanchuk, H. H. Strey and D. A. Hoagland, "Brownian motion of DNA confined within a two-dimensional array," Science **297**, 987–990 (2002).

[7] A. Milchev and K. Binder, "Static and dynamic properties of adsorbed chains at surfaces: Monte Carlo simulation of a bead-spring model," Macromolecules **29**, 343–354 (1996).

[8] R. Azuma and H. Takayama, "Diffusion of single long polymers in fixed and low density matrix of obstacles confined to two dimensions," J. Chem. Phys. **111**, 8666–8671 (1999).

[9] T. G. Desai, P. Keblinski, S. K. Kumar and S. Granick, "Molecular-dynamics simulations of the transport properties of a single polymer chain in two dimensions," J. Chem. Phys. **124**, 084904 (2006).

[10] T. G. Desai, P. Keblinski, S. K. Kumar and S. Granick, "Modeling diffusion of adsorbed polymer with explicit solvent," Phys. Rev. Lett. **98**, 218301 (2007).

[11] H.-J. Qian, L.-J. Chen, Z.-Y. Lu and Z.-S. Li, "Surface diffusion dynamics of a single polymer chain in dilute solution," Phys. Rev. Lett. **99**, 068301 (2007).

[12] D. Mukherji, G. Bartels and M. H. Müser, "Scaling laws of single polymer dynamics near attractive surfaces," Phys. Rev. Lett. **100**, 068301 (2008).

[13] J. Zhao and S. Granick, "Polymer lateral diffusion at the solid–liquid interface," J. Am. Chem. Soc. **126**, 6242–6243 (2004).

[14] R. B. Pandey, A. Milchev and K. Binder, "Semidilute and concentrated polymer solutions near attractive walls: Dynamic Monte Carlo simulation of density and pressure profiles of a coarse-grained model," Macromolecules **30**, 1194–1204 (1997).

[15] A. Chremos, E. Glynos, V. Koutsos and P. J. Camp, "Adsorption and self-assembly of linear polymers on surfaces: a computer simulation study," Soft Matt. **5**, 637–645 (2009).

[16] K. Kremer and G. S. Grest, "Dynamics of entangled linear polymer melts: A molecular-dynamics simulation," J. Chem. Phys. **92**, 5057–5086 (1990).

[17] S. Metzger, M. Müller, K. Binder and J. Baschnagel, "Adsorption transition of a polymer chain at a weakly attractive surface: Monte Carlo simulation of off-lattice models," Macromol. Theory Simul. **11**, 985–995 (2002).

[18] D. Frenkel and B. Smit, *Understanding Molecular Simulation*, 2nd ed. (Academic, San Diego, 2002).

[19] P.-G. de Gennes, *Scaling Concepts in Polymer Physics* (Cornell University Press, Ithaca, N.Y., 1979).

[20] A. M. Ferrenberg and R. H. Swendsen, "New monte carlo technique for studying phase transition," Phys. Rev. Lett. **61**, 2635–2638 (1988).

[21] S. J. Plimpton, "Fast Parallel Algorithms for Short-Range Molecular Dynamics," J. Comp. Phys. **117**, 1–19 (1995).

[22] S. A. Adelman and J. D. Doll, “Generalized Langevin equation approach for atom/solid-surface scattering: General formulation for classical scattering off harmonic solids,” J. Chem. Phys. **64**, 2375–2388 (1976).

[23] J. M. H. M. Scheutjens and G. J. Fleer, “Statistical theory of the adsorption of interacting chain molecules. 1. Partition function, segment density distribution, and adsorption isotherms,” J. Phys. Chem. **83**, 1619–1635 (1979).

[24] A. Milchev and K. Binder, “Polymer solutions confined in slit-like pores with attractive walls: An off-lattice Monte Carlo study of static properties and chain dynamics,” J. Comput. Aided Mater. Des. **2**, 167–181 (1995).

[25] A. Sikorski and I. Żukowska, “Dynamics of branched chain solutions in adsorbing slit. A Monte Carlo study,” Rheol. Acta **47**, 571–577 (2008).

[26] D. Mukherji and M. H. Müser, “Possible explanation of the λ-shape anomaly in polymer surface diffusion,” pre **74**, 010601(R) (2006).

[27] D. Mukherji and M. H. Müser, “Glassy dynamics, aging in mobility, and structural relaxation of strongly adsorbed polymer films: Corrugation or confinement?,” Macromolecules **40**, 1754–1762 (2007).

AUTHOR'S BIOGRAPHY

Wonki Roh was born in 1978 in Seoul, Korea. From 1996 to 2003 he studied at the Hanyang University, where he obtained a B.S. in Materials Engineering. During this time, he also served in the military from 1998 to 2000. In 2004 he began studying towards a Ph.D. in Materials Science and Engineering at the University of Illinois at Urbana-Champaign, where he joined Prof. Erik Luijten's computational materials research group. His research focused on using computer simulations to study the phase behavior of dipolar fluids and ion–dipole mixtures, and the surface diffusion of adsorbed polymers.